JGR Oceans

AGU ADVANCING EARTH AND SPACE SCIENCE

A Unified Breaking Onset Criterion for Surface Gravity Water Waves in Arbitrary Depth

Morteza Derakhti[1] ⓘⅮ , **James T. Kirby**[2] ⓘⅮ , **Michael L. Banner**[3] ⓘⅮ , **Stephan T. Grilli**[4] ⓘⅮ , and **Jim Thomson**[1] ⓘⅮ

[1] Applied Physics Laboratory, University of Washington, Seattle, WA, USA, [2] Center for Applied Coastal Research, Department of Civil and Environmental Engineering, University of Delaware, Newark, DE, USA, [3] School of Mathematics and Statistics, University of New South Wales, Sydney, New South Wales, Australia, [4] Department of Ocean Engineering, University of Rhode Island, Narragansett, RI, USA

Abstract We investigate the validity and robustness of the Barthelemy et al. (2018, https://doi.org/10.1017/jfm.2018.93) wave-breaking onset prediction framework for surface gravity water waves in arbitrary water depth, including shallow water breaking over varying bathymetry. We show that the Barthelemy et al. (2018) breaking onset criterion, which they validated for deep and intermediate water depths, also segregates breaking crests from nonbreaking crests in shallow water, with subsequent breaking always following the exceedance of their proposed generic breaking threshold. We consider a number of representative wave types, including regular, irregular, solitary, and focused waves, shoaling over idealized bed topographies including an idealized bar geometry and a mildly to steeply sloping planar beach. Our results show that the new breaking onset criterion is capable of detecting single and multiple breaking events in time and space in arbitrary water depth. Further, we show that the new generic criterion provides improved skill for signaling imminent breaking onset, relative to the available kinematic or geometric breaking onset criteria in the literature. In particular, the new criterion is suitable for use in wave-resolving models that cannot intrinsically detect the onset of wave breaking.

1. Introduction

Surface wave breaking is a highly dissipative process, transferring excess wave energy flux into currents and turbulence (Melville, 1996). Familiar breaking onset manifests as a crest-breaking event characterized by the formation of a multivalued free surface and entrainment of air bubbles into the water column (excluding microbreakers which do not entrain air). An important exception discussed below is surging breakers over very steep beaches, in which the wave crest remains relatively smooth and the initiation of instability occurs at the toe (leading edge) of the wave.

We introduce a new term, *breaking inception*, which identifies the critical time at which a wave crest-breaking event is initiated within the growing crest region. This precedes any of the familiar visible breaking onset signatures identified above by a finite time, typically a small fraction of the local wave period. It is shown below that the breaking inception time is crucial for predicting breaking onset and breaking strength in advance of their realization.

Finding a robust and universal diagnostic parameter that determines the onset of breaking for surface gravity waves, and its strength, is of substantial importance in the prediction of atmosphere-ocean exchanges, nearshore circulation and mixing, design of offshore and nearshore infrastructures, and so forth, but as yet the problem is not completely resolved.

Considerable effort has been made to find a robust and universal methodology to predict the onset of breaking gravity water waves in deep and intermediate depth water (Babanin et al., 2007; Banner & Peirson, 2007; Barthelemy et al., 2018; Craciunescu & Christou, 2019; Fedele et al., 2016; Song & Banner, 2002; Khait & Shemer, 2018; Pizzo & Melville, 2019; Saket et al., 2017; Saket et al., 2018; Shemer & Liberzon, 2014; Tian et al., 2008; Toffoli et al., 2010; Wu & Nepf, 2002). This and other aspects of wave breaking have been covered in several excellent reviews of the topic (Banner & Peregrine, 1993; Melville, 1996; Perlin et al., 2013). Recently, Perlin et al. (2013) have reviewed the latest progress on prediction of geometry, breaking onset,

and energy dissipation of steepness-limited breaking waves. The predictive parameters involved can be categorized as (i) geometric, (ii) kinematic, and (iii) dynamic criteria. As summarized in Perlin et al. (2013, section 3), none of the available criteria can distinguish between breaking and nonbreaking crests in a universal sense.

The situation becomes even more complex in shallow water, where waves evolve in response to interaction with seabeds of arbitrary, complex geometry. The inclusion of water depth d as an important factor in shallow water breaking leads to the identification of a convenient dimensionless parameter $\gamma = H/d$ (McCowan, 1894), where H is the local wave height. Further, analysis of breaking criteria for the simplest case of waves shoaling over a planar slope introduces the slope itself as a parameter. The effect of bottom slope m in combination with a measure of wave steepness has been studied by Iribarren and Nogales (1949), who defined a single combination $\xi_0 = m/\sqrt{H_0/L_0}$ based on offshore wave height H_0 and wavelength L_0, and Battjes (1974), who defined a similar surf similarity parameter $\xi_b = m/\sqrt{H_b/L_b}$, with the index b denoting values taken at the time when visible breaking commences. The surf similarity parameter has been found to be useful in discriminating between breaker types as well as in refining the prediction of breaking onset based on γ. The range of results in the literature is reviewed by Robertson et al. (2013), who list six types of dependency of γ_b on additional parameters such as m and ξ_0 and provide a table of 36 examples of published formulae for the estimation of γ_b. Robertson et al. concluded that a single, easily implementable relationship covering all breaking phenomena is still elusive.

Our approach in this paper is underpinned by the conceptual framework paper (Barthelemy et al., 2018) (hereafter B18) for predicting breaking onset, and its companion paper (Derakhti et al., 2018) (hereafter D18) for predicting breaking strength. These papers report the discovery of generic predictors for breaking onset and strength for 2-D and 3-D modulating waves in deep and intermediate depth conditions. We seek to validate that this framework is equally valid for predicting shallow water wave-breaking onset.

The local energy flux parameter $\boldsymbol{B}$ introduced by B18 is defined at the wave crest region as

$$\boldsymbol{B} = \mathscr{F}/E|\boldsymbol{C}| \qquad (1)$$

where $\mathscr{F} = \boldsymbol{U}(p + E)$ is the local flux of mechanical energy/unit volume, E is the mechanical energy/unit volume, and $\boldsymbol{U}$ is the local liquid velocity. The wave crest translates with propagation speed $C = |\boldsymbol{C}|$, which is generally time dependent. On the free surface, the pressure p is taken to be zero, reducing the expression for $\boldsymbol{B}$ to

$$B = U/C \qquad (2)$$

where U is the component of liquid velocity at the wave crest in the direction of wave propagation. Although Equation 2 appears similar to the kinematic breaking onset criterion (Perlin et al., 2013, section 3.2), it represents the normalized flux of mechanical energy at the crest, and thus should be considered as a dynamical criterion. The interested reader is referred to the discussion on line 21 on p. 466 of B18. In the linear approximation, B simplifies to $\gamma/2$ and the local wave steepness $S = kH/2$ (k is the wave number) in shallow and deep water, respectively.

B18 explains and validates the role of the parameter B (Equation 2) as a robust predictor of whether the crest of a steepening wave evolves to breaking, or whether it stops growing and continues to propagate without breaking. B18 shows that a wave crest will evolve to breaking if B tracked at the evolving wave crest transitions through a generic threshold B_{th}, which then sets the breaking inception time. D18 shows that the rate at which B normalized by the local wave period transitions through this generic threshold also sets the breaking strength or total energy dissipated by the breaking event. Should B not transition through B_{th}, that crest will not evolve to breaking. Thus, tracking B at the evolving crest has only two outcomes—either B fails to transition through B_{th}, in which case the crest will not evolve to breaking, or else the crest will evolve to breaking inception when B transitions through B_{th}, and will then evolve rapidly to visible breaking onset. This mirrors the physics of how breaking occurs. In this case, the normalized rate of change of B at the inception time provides a generic predictor of the breaking strength (D18), but this aspect of shallow water breaking is left for a companion paper in progress.

Based on numerical simulation of 2-D and 3-D focused wave packets in deep and intermediate depths, B18 found that a value of B_{th} in the range $[0.85, 0.86]$ provides a robust threshold that identifies imminent

breaking crest in 2-D and 3-D wave packets propagating in deep or intermediate uniform water depths. Subsequently, using a different modeling framework, D18 found consistent results for representative cases of modulated wave trains and focused packets in deep and intermediate depth water. These numerical findings for 2-D and 3-D cases were closely supported by the laboratory experiments of Saket et al. (2017, 2018) which include direct wind forcing.

It remains to determine whether the breaking threshold framework proposed by B18, that is, $B_{th} \approx 0.85$ as a generic threshold for predicting breaking, is also valid for waves in shallow water with relatively rapidly varying depth. Our goal is to investigate in detail to what extent the results reported by B18 and D18 for deep and intermediate water waves carry over to shallow water conditions. The utility of a predictor such as $B_{th} = 0.85$, rather than the classic $B_{th} = 1$, is its application in models that cannot directly resolve breaking and fail before waves reach $B = 1$.

We use a large-eddy-simulation (LES)/volume-of-fluid (VOF) model (Derakhti & Kirby, 2014a, 2016) and a 2-D fully nonlinear potential flow solver using a boundary element method (FNPF-BEM) (Grilli et al., 2014a; Grilli & Subramanya, 1996) to simulate nonlinear wave evolution, focusing on breaking onset behavior. Simulations are conducted for a variety of scenarios including regular, irregular, solitary, and focused waves shoaling over idealized bed topographies, including an idealized bar geometry and mildly to steeply sloping planar beaches. Additionally, we examine the applicability of the criterion for collapsing/surging breaking cases in shallow water, for which an instability leading to breaking may develop close to the toe (leading edge) of the wave front.

2. Computational Approaches

In this section, we provide a brief overview of the two modeling approaches used: the polydisperse two-fluid LES/VOF model of Derakhti and Kirby (2014a) based on the model TRUCHAS (Francois et al., 2006) and the FNPF-BEM model of Grilli et al. (1989) and Grilli and Subramanya (1996). The cases considered here are essentially 2-D in the (x, z) plane, allowing us to employ a purely 2-D version of FNPF-BEM. The FNPF-BEM model is not valid beyond the first onset of breaking and is thus only used below to consider the transient solitary wave cases.

As mentioned, the focus of this study is the examination of geometry, kinematics, and dynamics of an evolving crest up to the close vicinity of the visible breaking onset stage that is essentially before the start of the bubble entrainment process. However, in all simulation cases considered here, except the transient solitary wave cases, it is of interest to examine how an evolving crest interacts with decaying turbulence patches left behind from precedent breaking events. In addition, the LES/VOF model results are used for the examination of the wave-breaking-induced energy dissipation in a companion study. For these reasons, a relatively accurate postbreaking behavior of the simulation cases is needed, which then justifies the inclusion of bubble dynamics into our LES/VOF simulations.

Validation of the models for the present application is discussed in Appendix B.

2.1. The LES/VOF Model

The LES/VOF computations are performed using the Navier-Stokes solver TRUCHAS (Francois et al., 2006) with extensions of a polydisperse bubble phase and various turbulence models (Carrica et al., 1999; Derakhti & Kirby, 2014a; Ma et al., 2011). Details of the current mathematical formulations and numerical methods may be found in Derakhti and Kirby (2014a, section 2).

The filtered governing equations for conservation of mass and momentum of the liquid phase are given by

$$\frac{\partial \alpha \rho}{\partial t} + \frac{\partial \alpha \rho \tilde{u}_j}{\partial x_j} = 0, \tag{3}$$

$$\frac{\partial \alpha \rho \tilde{u}_i}{\partial t} + \frac{\partial \alpha \rho \tilde{u}_i \tilde{u}_j}{\partial x_j} = \frac{\partial \Pi_{ij}}{\partial x_j} - \alpha \rho g \delta_{3i} + \boldsymbol{M}^{gl}, \tag{4}$$

where $(i, j) = 1, 2, 3$; ρ is a constant liquid density; α and $\tilde{u}_i$ are the volume fraction and the filtered velocity in the i direction of the liquid phase, respectively; δ_{ij} is the Kronecher delta function; g is the gravitational acceleration; and $\Pi_{ij} = \alpha(-\tilde{p}\delta_{ij} + \tilde{\sigma}_{ij} - \tau_{ij})$ with $\tilde{p}$ the filtered pressure, which is identical in each phase due to the

neglect of interfacial surface tension, $\tilde{\sigma}_{ij}$ viscous stress and τ_{ij} the subgrid-scale (SGS) stress estimated using an eddy viscosity assumption and the Dynamic Smagorinsky model, which includes water/bubble interaction effects (for more details, see Derakhti & Kirby, 2014a, section 2.4). Finally, $\boldsymbol{M}^{gl}$ are the momentum transfers between liquid and gas phases, including the filtered virtual mass, lift, and drag forces (Derakhti & Kirby, 2014a, section 2.2).

Using the same filtering process as in the liquid phase, the equations for the bubble number density and continuity of momentum for each bubble size class with a diameter d_k^b, $k = 1, \ldots, N_G$, are then given by (Derakhti & Kirby, 2014a, section 2):

$$\frac{\partial N_k^b}{\partial t} + \frac{\partial \tilde{u}_{k,j}^b N_k^b}{\partial x_j} = R_k^b,$$ (5)

$$0 = -\frac{\partial \alpha_k^b \tilde{p}}{\partial x_j}\delta_{ij} - \alpha_k^b \rho^b g \delta_{3i} + \mathbf{M}_k^{lg},$$ (6)

where $\alpha_k^b = m_k^b N_k^b / \rho^b$, m_k^b, N_k^b and $\tilde{u}_{k,j}^b$ are the volume fraction, mass, number density, and filtered velocity in the j direction of the kth bubble size class; ρ^b is the bubble density; and R_k^b includes the source due to air entrainment in the interfacial cells (Derakhti & Kirby, 2014a, section 2.3), intergroup mass transfer, and SGS diffusion terms. Finally, $\mathbf{M}_k^{lg}$ represents the total momentum transfer between liquid and the kth bubble size class and satisfies $\mathbf{M}^{gl} + \sum_{k=1}^{N_G} \mathbf{M}_k^{lg} = 0$. In Equation 6, we neglect the inertia and shear stress terms in the gas phase following Carrica et al. (1999) and Derakhti and Kirby (2014a).

2.2. The FNPF-BEM Model

Equations for the 2-D FNPF-BEM model are briefly presented here. The velocity potential $\varphi(\mathbf{x}, t)$ is used to describe inviscid, irrotational flow in the vertical plane (x, z), with the velocity defined by $\mathbf{u} = \boldsymbol{\Delta}\varphi = (u, w)$. φ is governed by Laplace's equation in the liquid domain $\Omega(t)$ with boundary $\Gamma(t)$,

$$\Delta^2 \varphi = 0; \quad (x, z) \in \Omega(t)$$ (7)

Using the 2-D free space Green's function, $G(\mathbf{x}, \mathbf{x}_l) = -(1/2\pi)\log|\mathbf{x} - \mathbf{x}_l|$, and Green's second identity, Equation (7) is transformed into the boundary integral equation

$$\alpha(\mathbf{x}_l)\varphi(\mathbf{x}_l) = \int_{\Gamma(\mathbf{x})} \left[\frac{\partial \varphi}{\partial n}(\mathbf{x})G(\mathbf{x}, \mathbf{x}_l) - \varphi(\mathbf{x})\frac{\partial G(\mathbf{x}, \mathbf{x}_l)}{\partial n}\right] \, d\Gamma(\mathbf{x})$$ (8)

where $\mathbf{x} = (x, z)$ and $\mathbf{x}_l = (x_l, z_l)$ are position vectors for points on the boundary, $\mathbf{n}$ is the unit outward normal vector, and $\alpha(\mathbf{x}_l)$ is a geometric coefficient. Details of the surface and bottom boundary conditions and numerical methods may be found in Grilli et al. (1989) and Grilli and Subramanya (1996). The model provides instantaneous surface elevation and liquid velocity at the surface.

3. Model Configuration and Test Cases

3.1. Test Cases

Our numerical experiments are performed in a virtual wave tank with three different idealized bed geometries, illustrated in Figure 1. Cases include deep to shallow water transition conditions. We define the coordinate system (x, y, z) such that x and y represent the along-tank and transverse directions, respectively, and z is the vertical direction, positive upward, and measured from the still water level. We note that waves are usually breaking over the bar crest or the down-wave slope for cases of shoaling over a bar ($x > 0$ in Figure 1b).

All model simulations are performed with the model initialized with quiescent conditions. In the LES/VOF model, we specify the total instantaneous free surface, η_w, and liquid velocity, (u_w, w_w), at the model upstream boundary, (x_w, y, z), for various incident wave conditions, including regular sinusoidal, focused packets, modulated wave trains, and irregular waves propagating over a flat bed or over a bar geometry, as well as regular cnoidal waves shoaling over a plane beach. In the FNPF-BEM model, we specify solitary waves as initial condition on the free surface, using the elevation, potential and normal velocity derived from
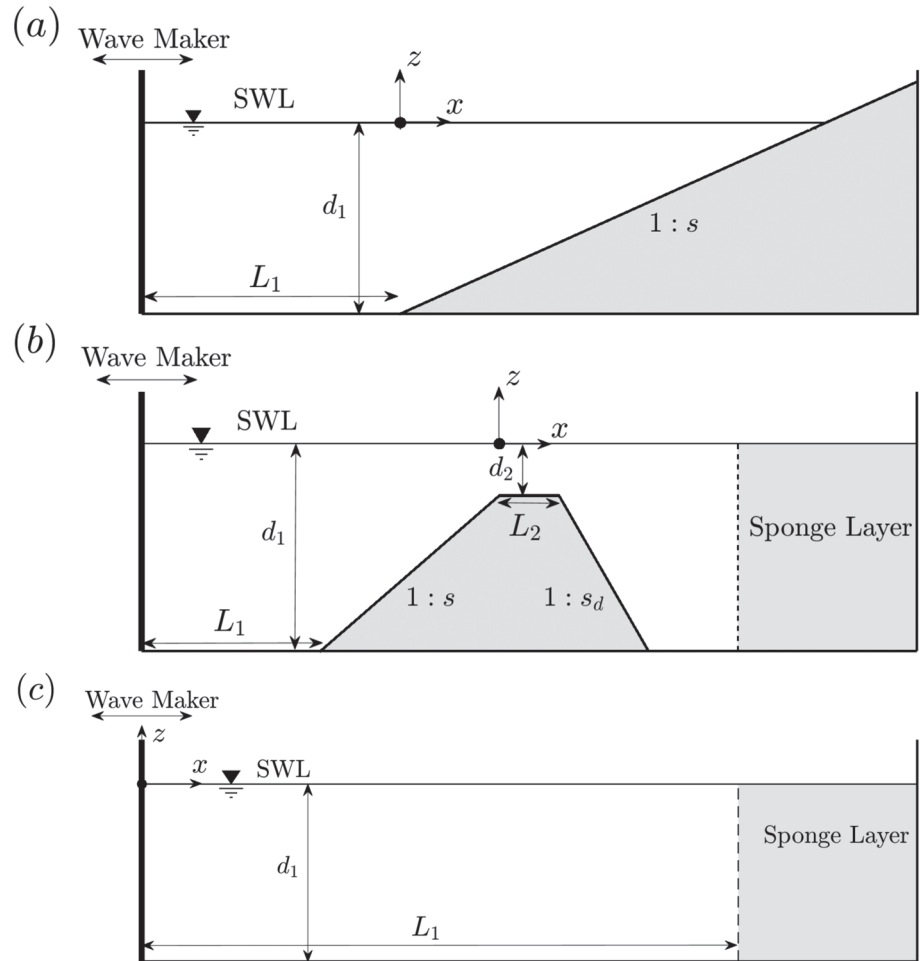
Figure 1. Schematic of the side view of the computational domain for the waves propagating over (a) a plane beach, (b) an idealized bar, and (c) a flat bed geometry.

the Tanaka (1986) solution. Table 1 summarizes the input parameters for all simulated cases.

In all simulated cases, the selected grid size in the x direction, Δx, is smaller than 1/100 of the wavelength in the vicinity of the initial breaking point or unbroken crest maximum. A uniform grid of $\Delta y = \Delta z = \Delta x/2$ is used for the simulated LES/VOF cases, with the total number of grid points that varies between 0.5×10^6 and 3×10^6. The CPU run-time of the LES/VOF simulations is typically less than a day for a 100-s simulation time using 200 processors on an HPC cluster.

3.1.1. Focused Wave Packets

The input focused wave packet was composed of $N = 32$ sinusoidal components of steepness $a_n k_n, n = 1, \ldots, N$, where a_n and k_n are the amplitude and wave number of the nth frequency component. The steepness of individual wave components is taken to be constant across the spectrum, or $a_1 k_1 = a_i k_i = \ldots = a_N k_N = S_g/N$ with $S_g = \sum_{n=1}^{N} a_n k_n$ taken to be a measure of the wave train global steepness. Based on linear theory, the free surface elevation at the wavemaker ($x = x_w$) for 2-D wave packets focusing at $x = x_f$ is given by (Derakhti & Kirby, 2014a; Rapp & Melville, 1990)

$$\eta_w = \sum_{n=1}^{N} a_n \cos[2\pi f_n(t - t_f) + k_n(x_f - x_w)] \tag{9}$$

where f_n is the frequency of the nth component, x_f and t_f are the predefined, linear theory estimates of location and time of the focal point, respectively. The discrete frequencies f_n are uniformly spaced over the band $\Delta f = f_N - f_1$ with the central frequency defined by $f_c = 1/2(f_N + f_1)$.

Table 1
Input Parameters for the Simulated Cases

Case	H_w (mm) (or S_g)	T_w (s)	d_1 (m)	L_1 (m)	s	ξ_0 (or $\Delta f/f_c$)	d_2 (m)	L_2 (m)	s_d
P1-r-LV	80, 120, 180, 200, 240	4.0	0.5	0	5	$3.9 - 2.3$	—	—	—
P2-r-LV	150	4.0	0.5	0	10	1.43	—	—	—
P3-r-LV	40, 150	4.0	0.5	0	20	1.38, 0.71	—	—	—
P4-r-LV	90, 150, 200	4.0	0.5	0	40	0.46 - 0.31	—	—	—
P5-r-LV	90, 150	4.0	0.5	0	100	0.18, 0.14	—	—	—
P6-r-LV	90, 120, 150	4.0	0.3	0	200	0.09 - 0.07	—	—	—
P7-s-LV	240, 260, 270, 350, 500	—	1.0	6.0	8	—	—	—	—
P7-s-BM	240	—	1.0	20.0	8	—	—	—	—
P8-s-BM	300, 450, 600	—	1.0	20.0	15	—	—	—	—
P9-s-BM	200, 600	—	1.0	20.0	100	—	—	—	—
B1-r-LV	41, 43, 46, 46.2, 46.3, 46.5, 47, 50, 53, 59	1.01	0.4	6	20	$0.30 - 0.25$	0.1	2	10
B2-r-LV	47, 50, 53, 59	1.01	0.4	6	100	0.06 - 0.05	0.1	2	10
B3-r-LV	24, 26, 26.5, 27, 27.5, 30, 34, 40	2.525	0.4	6	20	$1.05 - 0.81$	0.1	2	10
B4-r-LV	26, 30, 30.5, 31, 32, 34, 40	2.525	0.4	6	100	$0.21 - 0.16$	0.1	2	10
B5-f-LV	(0.20, 0.21, 0.22, 0.23, 0.30)	T_c : 1.14	0.6	3	20	(0.75)	0.2	3	10
B6-i-LV	H_{rms} : 40	T_p : 1.7	0.47	0	20	0.52	0.12	2	10
B7-i-LV	H_{rms} : 40	T_p : 1.7	0.47	0	20	0.52	0.17	2	10
B8-s-BM	36, 40, 46, 46.6, 47, 60, 80	-	0.4	8	20	—	0.1	2	10
F1-f-LV	(0.25, 0.3, 0.302, 0.31, 0.32, 0.42, 0.44, 0.46)	T_c : 1.14	0.6	16	—	(0.75)	—	—	—
F2-f-LV	(0.32, 0.36, 0.40)	T_c : 1.33	0.6	22	—	(1.0)	—	—	—
F3-m-LV	(0.160, 0.176)	T_c : 0.68	0.55	64	—	(0.0954)	—	—	—

Note. Each case identifier has 3 parts indicating the geometry of the wave tank (P: planar beach, B: barred beach, F: flat bed; numbers: various geometry parameters), the type of the incident waves (r: regular, i: irregular, s: solitary waves, f: focused packets, m: modulated wave trains), and the numerical model (LV: LES/VOF, BM: FNPF-BEM), respectively. Here, H_w and T_w are the wave height and period of the regular waves at the wavemaker, and $\xi_0 = s^{-1}/\sqrt{H_0/L_0}$ is the surf-similarity parameter (Battjes, 1974); the rest of the variables are defined in Figure A1.

3.1.2. Modulated Wave Trains

For cases of modulated wave trains, we use the bimodal wave approach of Banner and Peirson (2007), with free surface elevation at the wavemaker given by

$$\eta_w = a_1 \cos(\omega_1 t) + a_2 \cos\left(\omega_2 t - \frac{\pi}{18}\right), \tag{10}$$

where $\omega_1 = 2\pi f_1$, $\omega_2 = \omega_1 + 2\pi\Delta f$, $S_g = a_1 k_1 + k_2 a_2$ and $a_2/a_1 = 0.3$. Increasing the global steepness S_g increases the strength of the resulting breaking event in both focused packets and modulated wave trains.

3.1.3. Irregular Wave Trains

For irregular wave cases, η_w is prescribed using the first $N = 2{,}500$ Fourier components of the measured free surface time series at the most offshore gauge of the cases experimentally studied by Mase and Kirby (1992) with $T_p = 1.7$ s, given by

$$\eta_w = \Sigma_{n=1}^{N} a_n \cos(\omega_n t + \epsilon_n) \tag{11}$$

where a_n and ϵ_n are the amplitude and phase of the nth Fourier component based on the measured free surface time series, and ω_n is the angular frequency of the nth Fourier component. Mase and Kirby (1992)

specified wavemaker conditions for irregular waves based on a Pierson-Moskowitz spectrum. Waves then propagated shoreward over a sloping planar beach. Here the same incident waves are used but shoal over an idealized bar. Liquid velocities for each spectral component are calculated using linear theory and then superimposed linearly at the wavemaker. No correction for second-order effects was made.

3.1.4. Regular Weakly Dispersive, Nonlinear Waves

For cnoidal waves, we use the theoretical relations for η_w and (u_w, w_w) as given in Wiegel (1960). Initial conditions for solitary wave tests were specified using the solution for finite amplitude waves due to Tanaka (1986). This initial condition represents a very accurate numerical solution to the full Euler equations and is more suitable for use here with the fully nonlinear numerical codes being used than the standard first-order Boussinesq solitary wave solution (e.g., Grilli & Subramanya, 1996).

3.2. Definition of a Breaking Crest

The visible manifestation of surface wave breaking events, excluding microbreakers, is the formation of a multivalued free surface, which is accompanied by the initiation of wave-breaking-induced energy dissipation and entrainment of air bubbles into the water column. In most wave-breaking modes, the breaking process initiates visibly at the crest of the breaking wave. Exceptions include surging breakers over very steep beaches in which the crest of the wave remains relatively smooth and the initiation of instability occurs at the toe (leading edge) of the wave.

Here, we consider an individual evolving crest to be a breaking crest if the initiation of multivalued free surface occurs in the crest region, for example, developing a vertical tangent on the forward face of the crest, followed rapidly by a spilling or plunging plume surging from the crest down the forward face. In all breaking crests considered here, the onset of breaking occurs fairly rapidly after a vertical tangent becomes apparent onshore of the crest.

In the FNPF-BEM framework, there is no dissipation mechanism in the model, and the model becomes unstable fairly rapidly after a vertical tangent becomes apparent at or near the crest, and a breaker jet starts forming. Thus, as was proposed in earlier work (e.g., Grilli et al., 1997), an individual crest in simulations using the FNPF-BEM model is also denoted as a breaking crest when the free surface slope at any given point on the front face of the wave (i.e., onshore of the crest) becomes vertical; a multivalued free surface elevation will typically occur at the next time step of computations.

4. Results

In this section, we examine in detail the onset of breaking on the basis of the parameter $B = U/C$ (Equation 2) for representative breaking and nonbreaking incident waves in intermediate depth and shallow water. The results for steepness-limited wave breaking in both focused packets and modulated wave trains (D18) are also presented. In the following section (section 5.2), we show that several geometric criteria for predicting the onset of breaking are not uniformly robust.

Figures 2a, 2d, and 2g show examples of the computed temporal variation of C from shallow to deep water, in which values of C are normalized by their corresponding values at the time $t^* = 0$ marking either the time when $B = 0.85$ or, for nonbreaking cases, the occurrence of maximum crest elevation. In this and subsequent plots, the color black for curves or points indicates cases where breaking occurs, while orange indicates nonbreaking cases. Figures 2b, 2e, and 2h show results for an estimate of phase speed c based on an approximate nonlinear dispersion relation as $c = \sqrt{gk^{-1}\tanh[k(d + H_c)]}$, which is slightly different than that proposed by Booij (1981) (replacing $H/2$ by the crest height H_c). The behavior of crest translation speed C is seen to be distinctly different from estimates based on dispersion relations for regular waves. The results show that the ratio c/C around $t^* = 0$ ranges between 0.8 and 1.1 in most cases.

We note that C is obtained by calculating the rate of change of the horizontal location of an evolving crest, for example, x_{η_c} if the crest is propagating in the x direction. In both FNPF-BEM and LES/VOF frameworks, x_{η_c} may occur between the grid locations, and thus a local fitting (or smoothing) to the predicted free surface locations $(\eta(x, y, t))$ is needed to obtain a robust estimate of x_{η_c} for each evolving crest. Such local fitting (or smoothing) also removes the potential noise in the calculated C values due to the existence of local maxima in the crest region due to the presence of relatively high frequency waves, especially when they are propagating in the direction opposite to that of the dominant wave. Although implementing local fitting (or smoothing) for predicted maximum η values and their locations significantly improves the estimation of C,
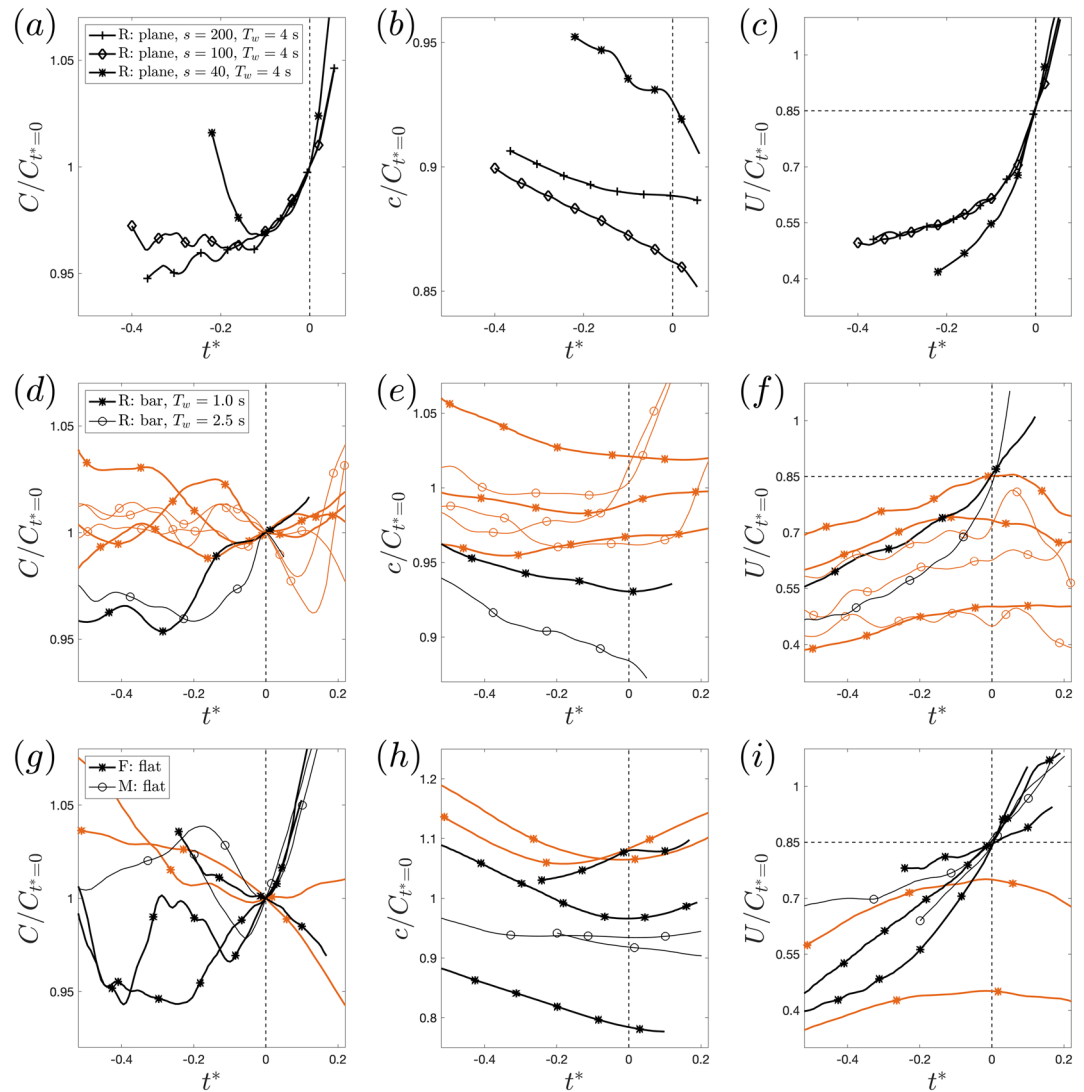
Figure 2. Examples of the temporal variation of (a, d, g) the crest propagation speed C, (b, e, h) phase speed $c = \sqrt{gk^{-1}\tanh[k(d + H_c)]}$, and (c, f, i) the horizontal particle velocity at the crest U, all normalized by the corresponding C value at $t^* = 0$, for breaking (black symbols and lines) and nonbreaking (orange symbols and lines) crests in (a, b, c) regular waves (R) shoaling over a plane beach with slope $m = 1/s$, (d, e, f) regular waves (R) propagating over a bar, and (g, h, i) focused packets (F) and modulated wave trains (M) in deep and intermediate water.

in some cases there are still some small undulations in the C values (as shown in the left column of Figure 2) obtained from tracking the location of η_c (e.g., $C = dx_{\eta_c}/dt$). For unsteadily evolving dispersive wave packets, the generic crest slowdown mechanism results in a systematic variability in C (see, e.g., Banner et al., 2014, for more details).

In addition, the estimation of C will be challenging in cases in which the crest region is relatively flat. One clear example of such cases is the time at which an evolving crest reaches the shoreline and the wave rapidly surges up-slope without overturning; such cases are detailed later in the text. Considering these uncertainties, we can write $C = C_e \pm \Delta C$ where C_e is the exact propagation speed of the evolving crest and ΔC represents the corresponding uncertainty estimate. The results of the temporal variation of C (e.g., Figures 2a, 2d, and 2g) suggest that $\Delta C/C_e < 0.01$ prior to $t^* = 0$ in the simulated cases in which the crest region has a resolved curvature in the considered discretization.

In the FNPF-BEM model, U is the actual particle velocity on the free surface at the wave crest. In the LES/VOF model, we set U as the maximum of the computed horizontal near-surface velocity over the computational cells in the range $x_{\eta_c} \pm 3\Delta x$. We also perform a simple smoothing, using the moving average

method, on the U time series for each evolving crest before calculating B values. Figures 2c, 2f, and 2i show examples of the temporal evolution of U normalized by their corresponding C values at the time $t^* = 0$, $C_{t^*=0}$. In Figure 2, all C, c, and U values that correspond to an evolving crest are normalized by a single value $C_{t^*=0}$, the propagation speed of the crest at the time $t^* = 0$. Thus, $U/C_{t^*=0}$ is not equal to B for $t^* \neq 0$. Our results show that U significantly increases as an evolving crest approaches the break point $t^* = t_b^*$ (which typically occurs in the range $[0, 0.2]$), as opposed to C, which varies by less than 5% in the range $-0.4 < t^* < t_b^*$ for cases of shoaling over gentle to moderate slopes or cases in deep and intermediate depth water. For these cases, the results suggest that the variation in B is mainly related to variation in U in the range $-0.4 < t^* < t_b^*$.

We also write U in terms of the exact value (U_e) and an uncertainty estimate (ΔU), $U = U_e \pm \Delta U$, in which the results indicate that $\Delta U/U_e < \Delta C/C_e$ for most cases. Thus, we can write

$$B = \frac{U_e \pm \Delta U}{C_e \pm \Delta C} = \frac{U_e}{C_e} \times \frac{1 \pm \Delta U/U_e}{1 \pm \Delta C/C_e} = B_e(1 \pm \Delta U/U_e)\left(1 \pm \Delta C/2C_e + O([\Delta C/C_e]^2)\right). \quad (12)$$

where B_e represents the exact value of B, and then the uncertainty in the estimated B values, denoted by ΔB, reads in relative value as

$$\pm \Delta B/B_e = \pm \Delta U/U_e \pm \Delta C/2C_e + O([\Delta C/C_e]^2, [\Delta C/C_e][\Delta U/U_e]). \quad (13)$$

Based on these results and taking $\Delta U/U_e < \Delta C/C_e < 0.01$, the uncertainty in the estimated B values from our numerical experiments (described below) will be $\Delta B/B_e < 0.015$ for the cases in which the crest region has a resolved curvature in the considered discretization. In particular, $\Delta B < 0.013$ for B values approaching the breaking inception threshold value B_{th}, which varied in the range $[0.85, 0.86]$ in the numerical cases of B18. Further, Saket et al. (2017,2018) reported an uncertainty estimation of $\Delta B = 0.020$ for their experimental measurements.

4.1. Results for Waves Shoaling Over a Plane Beach

Figure 3 shows examples of the evolution of regular waves (with $T_w = 4$ s) over a plane beach with a slope $m = 1/s$; including shoaling, breaking onset, and progression of breaking crests; and the corresponding temporal variation of the breaking onset parameter B for the tracked crests. The incident waves cover a wide range of ξ_0 values, demonstrating a transition from spilling breaking, frames (a and b), to collapsing and surging breaking, frames (g–j). We observe that B always transitions through the breaking inception threshold value $B_{\mathrm{th}} \approx 0.85$ prior to visible crest breaking in cases in which breaking is due to the initiation of instability in the crest region (i.e., spilling or plunging breakers). In these cases, we also observe that B exceeds 1 shortly after the breaking inception threshold value $B_{\mathrm{th}} \approx 0.85$ is transitioned, and the time scale $\Delta t_{\mathrm{onset}} = t_{B=1} - t_{B=B_{\mathrm{th}}}$ is a decreasing function of ξ_0 for breaking waves with the same wave period (T_w here). Note that in shorebreaks, $\Delta t_{\mathrm{onset}}$ is relatively small and estimating B is challenging due to rapid changes, uncertainty, and ambiguity in defining x_{η_c} after $B = B_{\mathrm{th}}$ is transitioned. For example, in the shorebreak case shown in frames (g and h), the calculation of B is terminated before reaching $B = 1$ due to a poor estimation of C as the wave transitions through the time at which $B = B_{th}$. Frames (i) and (j) show the results for two cases with $\xi_0 = 2.26$ and 2.61 surging over a slope of $1/5$ or slope angle $11.31°$. In both cases, the initiation of instability occurs at the toe of the wave, and the maximum B values remain below B_{th}.

Figure 4 shows similar results to those of Figure 3 for solitary wave cases shoaling over steep beaches simulated using the FNPF-BEM (dashed lines) and LES/VOF (solid lines) models. Here and subsequently, dashed and solid lines represent results of simulations using the FNPF-BEM and LES/VOF models, respectively. Breaking of solitary waves on plane slopes from $1/100$ to $1/8$ was studied using the FNPF-BEM model by Grilli et al. (1997), who reported no breaking for slopes greater than $12°$. Using a least squares error method based on their numerical experiments, Grilli et al. (1997) proposed a maximum limit for nonbreaking solitary waves shoaling on a slope $m = 1/s$ given by $H_w^m = 16.9d_1/s^2$. They also introduced a parameter $\zeta_0 = 1.521/s\sqrt{H_w/d_1}$ and characterized the type of their breaking cases based on ζ_0 as surging when $0.30 < \zeta_0 < 0.37$, plunging when $0.025 < \zeta_0 < 0.30$, and spilling when $\zeta_0 < 0.025$.

Figure 4a shows the FNPF-BEM model results for the evolution of a plunging breaking solitary wave on a slope $1/15$ with $H_w = 0.30$ m $> H_w^m = 0.08$ m and $\zeta_0 = 0.19$ ($d_1 = 1$ m). Frames (c) and (e) show results of the LES/VOF model for two cases on a slope $1/8$ ($H_w^m = 0.264$) with $H_w = 0.50$ m ($\zeta_0 = 0.27$)
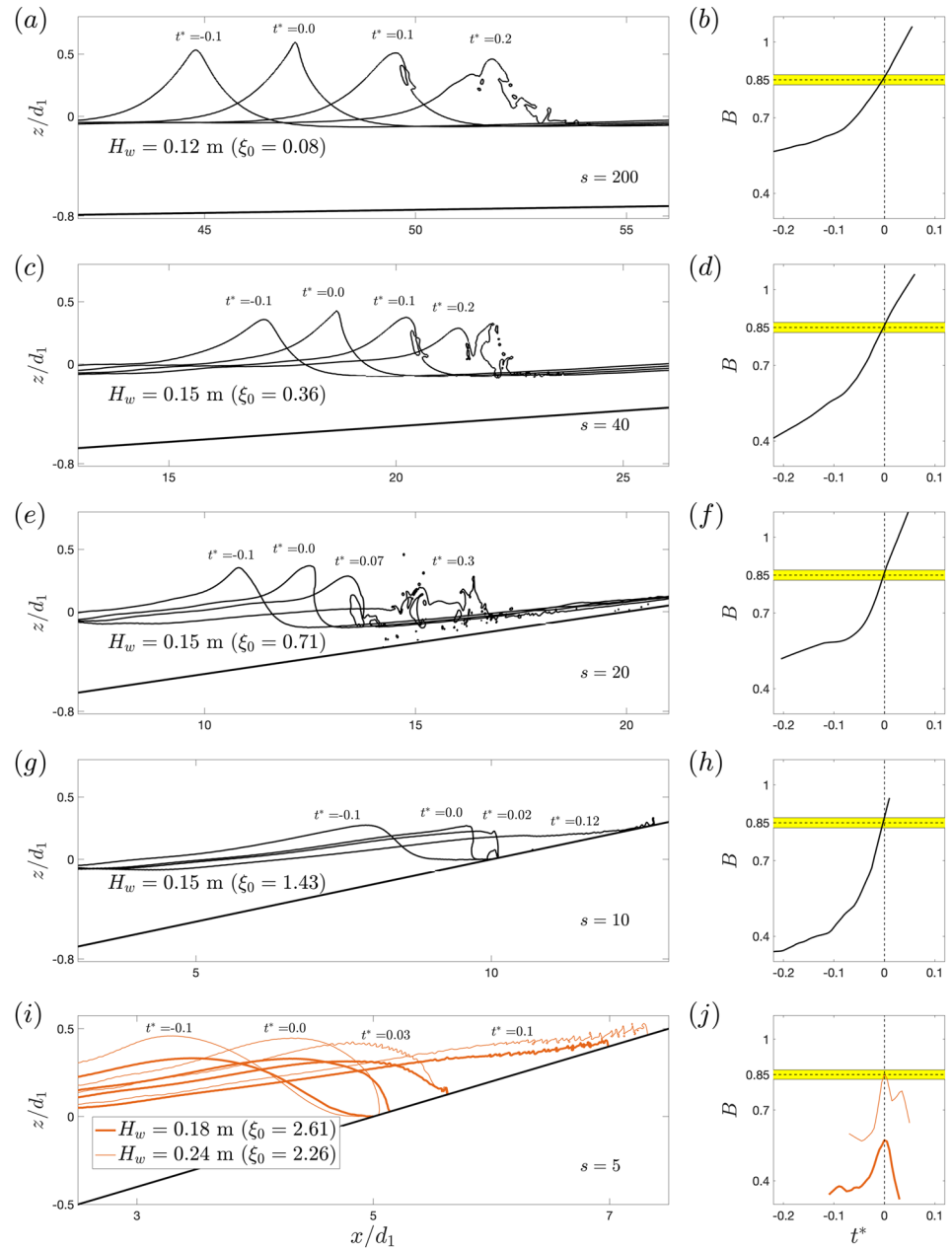
Figure 3. (a, c, e, g, i) Snapshots of free surface elevations and (b, d, f, h, j) temporal evolution of the breaking onset parameter B for regular waves ($T_w = 4$ s) propagating over a plane beach with a slope $m = 1/s$, demonstrating a transition from spilling to collapsing and surging breaking with an increasing $\xi_0 = s^{-1}/\sqrt{H_0/L_0}$ (see Table 1). Here d_1 is the still water depth at the beginning of the plane slope segment (Figure 1a). Cases without an apparent overturning crest are indicated in orange. All results are obtained using the LES/VOF model. The yellow regions indicate $B = 0.85 \pm 0.02$.

and $H_w = 0.35$ ($\zeta_0 = 0.32$). For all three cases shown in frames (a–f), the occurrence and breaking type of the incident solitary waves predicted by both the FNPF-BEM and LES/VOF models are consistent with the predictions from H_w^m and ζ_0 (Grilli et al., 1997). In all three cases, we observe that the corresponding B parameter reaches 0.85 close to a time at which a vertical tangent appears on the crest front face. As in Figure 3, we also observe that B exceeds 1 shortly after B_{th} is transitioned for all breaking solitary waves, and the time scale $\Delta t_{onset} = t_{B=1} - t_{B=B_{th}}$ is a decreasing function of ζ_0, consistent with the trend observed for regular waves with respect to ξ_0 (Figure 3).
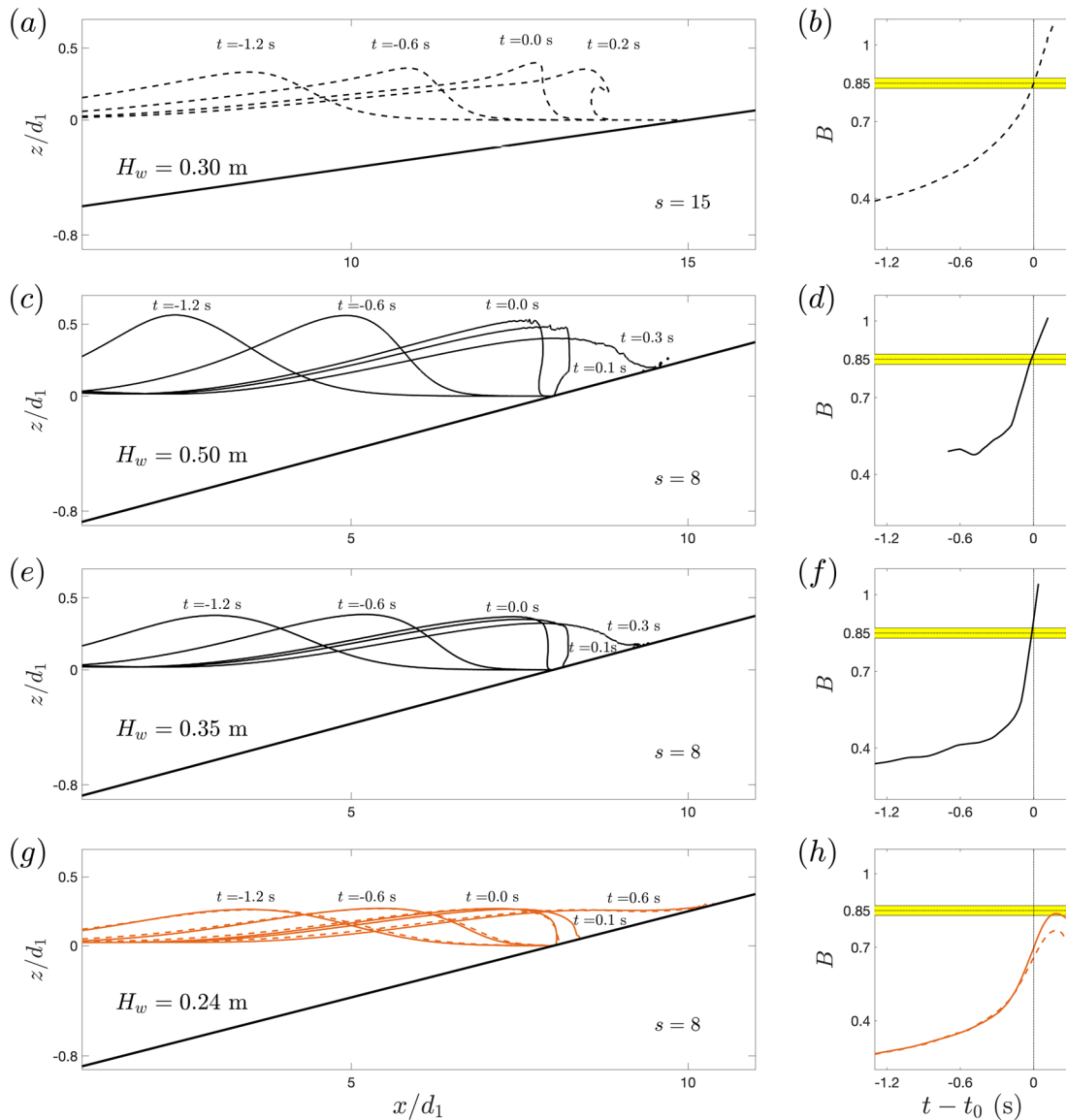
Figure 4. (a, c, e, g) Snapshots of the free surface elevations and (b, d, f, h) the temporal evolution of the breaking onset parameter B for solitary waves propagating over a plane beach with a slope $m = 1/s$. Dashed and solid lines represent the results for cases simulated using the FNPF-BEM and LES/VOF models, respectively. The yellow regions indicate $B = 0.85 \pm 0.02$.

Figure 4g shows the evolution of a nonbreaking solitary wave on a slope 1/8 with $H_w = 0.24$ m $< H_w^m = 0.264$ m predicted by both the FNPF-BEM and LES/VOF models. Frame (h) shows the calculated B curves from both model results. In this case, t_0 represents the time of occurrence of maximum crest elevation, as opposed to Frames (a–f) in which t_0 represents the time when $B = 0.85$. The maximum B values, B_m, from both models remain below B_{th}; however, B_m calculated from the FNPF-BEM model, is $\approx$6% smaller than that from the LES/VOF model results.

Figure 5 shows the temporal variations of x_{n_c}, C and U predicted by both models. The maximum difference between C and U values predicted by each model is $\approx$4%. Before the time at which the crest maximum is reached ($t < t_0$), U from the FNPF-BEM model is almost the same as that predicted by the LES/VOF model except close to the crest maximum time, where the difference between the two predictions reaches 1%. The FNPF-BEM model prediction for C is smaller and greater than that predicted by the LES/VOF model for $t < t_0$ and $t > t_0$, indicating that the BEM-predicted wave crest is pitching forward somewhat more slowly than the LES/VOF-predicted crest. The discrepancy in the corresponding B values is a maximum after $t > t_0$, with a value of $\approx$6%. The discrepancy between the FNPF-BEM and LES/VOF results is partly due to their
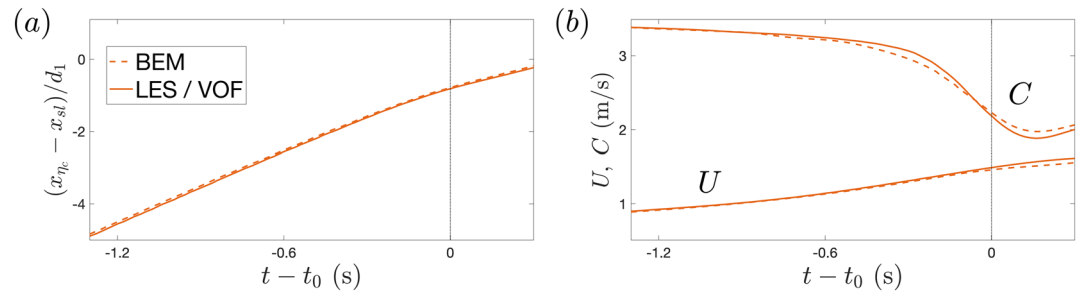
Figure 5. Temporal evolution of (a) x_{η_c} the horizontal location of the crest, and (b) C crest propagation speed and U particle horizontal velocity at the crest for the nonbreaking solitary wave shown in Figure 4g. Dashed and solid lines show results of simulations cases with the FNPF-BEM and LES/VOF models, respectively. Here x_{sl} is the cross-shore location of the shoreline.

different spatial resolution ($\Delta x_{\mathrm{BEM}} \approx 13\Delta x_{\mathrm{LES/VOF}}$) and the neglect of bed friction and viscous effects in the FNPF-BEM model. Further, a part of the discrepancy is related to the uncertainty in the estimation of C as the crest region becomes relatively flat, particularly for surging/shorebreak cases. Overall, we find that the two modeling approaches provide consistent estimates of liquid velocity and crest geometry evolution in cases where adequate spatial and temporal resolutions are used. This conclusion is further supported by the general consistency observed between intermediate and deep water results in the studies of B18 and D18, and contrasts with the negative evaluation of the LES/VOF approach made in Pizzo and Melville (2019). This is further supported by validations presented in the Appendix B.

4.2. Results for Waves Shoaling Over an Idealized Bar

As mentioned in section 1, the breaking inception threshold value $B_{\mathrm{th}} \approx 0.85$ may be considered as the indicator of breaking onset, with any wave for which B exceeds B_{th} inevitably breaking visibly a short time ($\Delta t_{\mathrm{onset}}$) later. However, one still needs to closely examine the behavior of B in the transition from breaking to nonbreaking cases in shallow water, including marginal breaking events, to confirm the validity of the breaking inception threshold value $B_{\mathrm{th}} \approx 0.85$ in a universal sense.
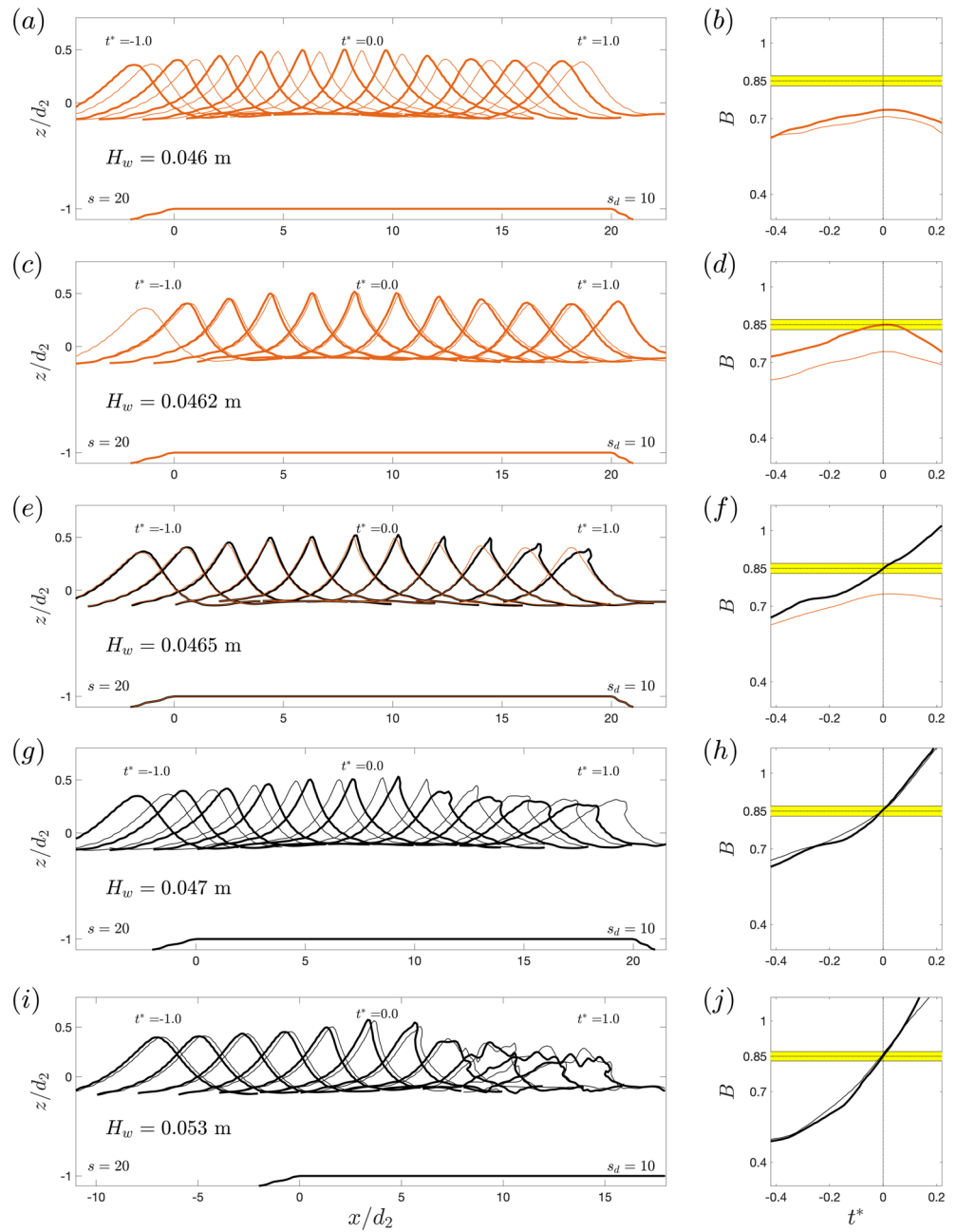
The transition from breaking to nonbreaking of shoaling waves over a plane beach may only occur close to the shoreline, where an accurate estimation of B is challenging, as discussed above. Thus, we consider the behavior of B for regular, irregular, and solitary waves, as well as focused packets, propagating over a submerged bar (Figure 1b), with an emphasis on marginally breaking cases. In the following, we present and discuss the computed temporal variation of B for cases of simulated regular and solitary waves. Cases with irregular waves and focused wave packets will be reported elsewhere.

Figure 6 shows the temporal evolution of two evolving crests and their corresponding B values for nonbreaking and breaking regular waves ($T_w = 1.01$ s) propagating over a submerged bar, as defined in Figure 1b. Each row shows LES/VOF results for a case with an initial wave height H_w, where increasing H_w results in a transition from nonbreaking (frames a–d) to intermittent breaking (frames e and f) and breaking (frames g–j) events. For each individual evolving crest, the reference time is the time at which B transitions through 0.85 or reaches its maximum for breaking and nonbreaking cases, respectively. Although incident crests with the same H_w have exactly the same initial wave conditions, their kinematics and dynamics near the break point or crest maximum are not the same, due to their interaction with the low-frequency waves in the numerical tank (e.g., seiches), the residual motions due to preceding waves, and so forth. Although these variations have a relatively small effect on the height of the evolving crests, they may result in an intermittent breaking, as shown in frames (e) and (f).

Figure 7 shows similar results as in Figure 6 but for the solitary wave cases, computed using the FNPF-BEM model. Results shown in Figures 6 and 7 confirm the validity of $B_{\mathrm{th}} \approx 0.85$ as a robust predictor of breaking onset in shallow water.

### 4.3. Summary of the Results

Figure 8 shows the variation of the maximum B values as a function of the wave Froude number F (defined in section 5.1 below) for all simulated crests, using LES/VOF and FNPF-BEM models, from deep to shallow water. As mentioned above, we observe that if B transitions through the

Figure 6. Temporal evolution of (a, c, e, g, i) wave profiles and (b, d, f, h) the breaking onset parameter B for two different evolving crests of a regular wave ($T_w = 1.01$ s) propagating over a bar with a front slope $m = 1/s$, demonstrating a transition from nonbreaking to spilling breaking with an increasing ξ_0. Here d_2 is the still water depth over the top of the bar (Figure 1b). All results are obtained using the LES/VOF model. The yellow regions indicate $B = 0.85 \pm 0.02$.

threshold value $B_{\text{th}} \approx 0.85$ it will attain the level $B = 1$ when the surface signatures of breaking appear for all cases. The two exceptional breaking wave cases indicated by + signs below $B = 1$ represent solitary wave cases simulated using the FNPF-BEM model, where the simulations stop before breaking onset due to insufficient spatial resolution. We observe that the breaking inception threshold values B_{th}, beyond which the crest evolves to breaking, range between 0.85 and 0.88 in shallow water wave breaking. This is consistent with the relevant previous studies of the variation
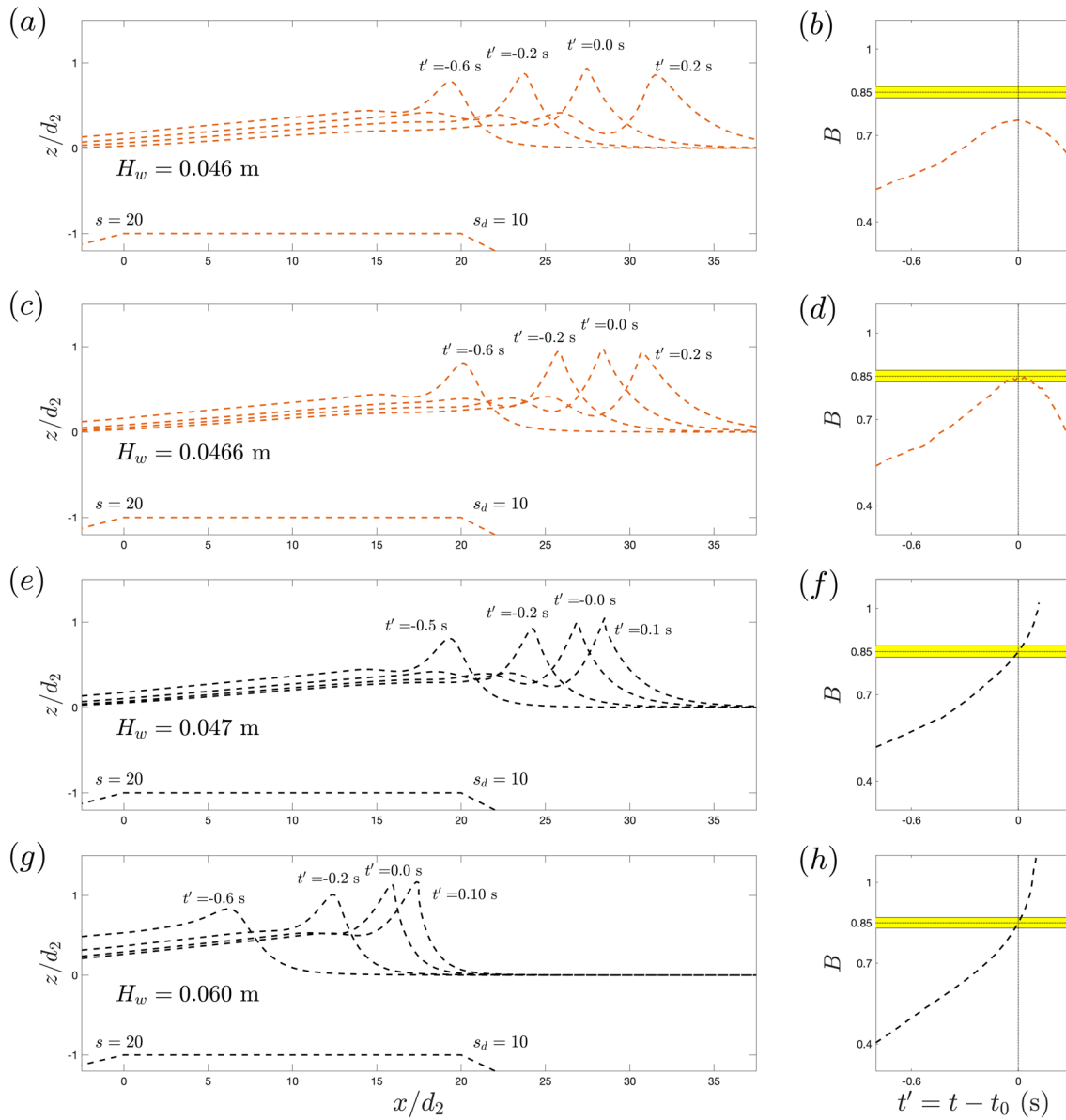
Figure 7. (a, c, e, g) Snapshots of the free surface elevations and (b, d, f, h) temporal evolution of the breaking onset parameter B, for solitary waves propagating over a bar with a front slope $m = 1/s$ demonstrating a transition from nonbreaking to spilling breaking with an increasing initial wave height. Here d_2 is the still water depth over the top of the bar (Figure 1b). All results are obtained using the BEM model. The yellow regions indicate $B = 0.85 \pm 0.02$.

of B_{th} in intermediate depth and deep water (Barthelemy et al., 2018; Derakhti et al., 2018; Saket et al., 2017, 2018). The plot also displays a dotted line corresponding to the linearized relation $B = F$. We observe that the maximum occurring values of B for all the tabulated steep but nonbreaking crests greatly exceed this lower limit, due to a combination of underprediction of fluid velocity in the crest as well as possible reductions of crest speed prior to breaking in intermediate depth cases.

5. Discussion

In this section, we present an evaluation of the other existing breaking criteria from the literature. These are the various geometric parameters defined below, which are applied to the simulated wave trains. Next, we comment on the extension of the results to 3-D shoaling and breaking waves in shallow water. Finally, we discuss the implementation of the parameter B in energy-conserving phase-resolving models.
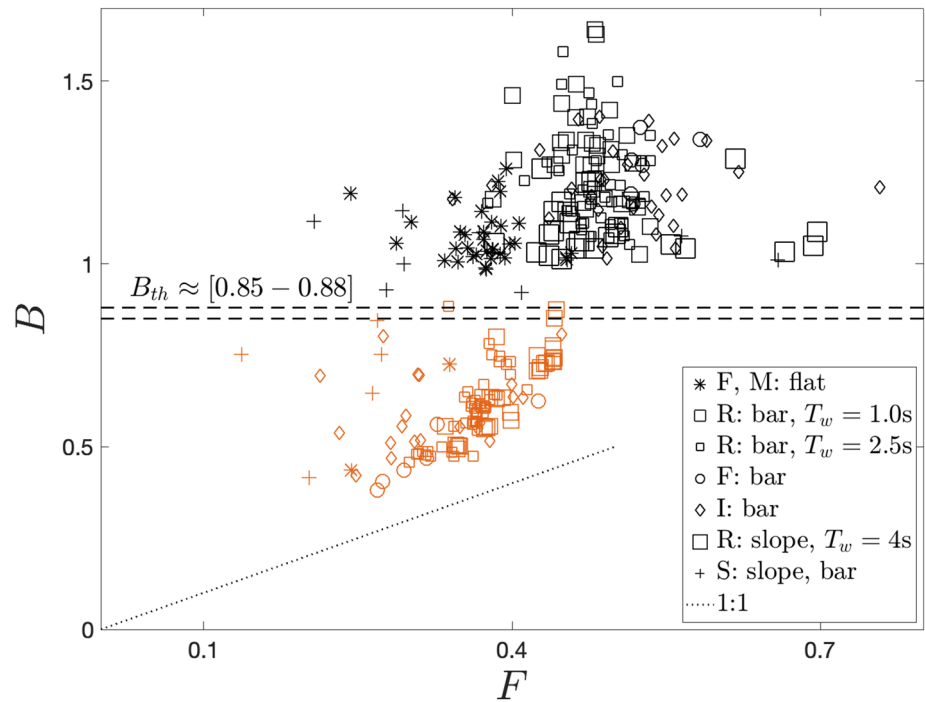
Figure 8. Maximum value of the breaking onset parameter B as a function of the wave Froude number F, for all breaking (black symbols) and nonbreaking (orange symbols) wave crests. In the breaking cases, the maximum value of B corresponds to the time, after the onset of breaking, at which the location of the crest maximum becomes noisy.

5.1. Definition of Local Geometric Parameters Used in the Analysis

Following Beji (1995), we define a wave Froude number

$$F = gH/2c_{\text{lin}}^2, \tag{14}$$

where $c_{\text{lin}}^2 = gk^{-1}\tanh kd$ and $k = 2\pi/L$ is the local wave number. We note that F simplifies to the nonlinearity parameter $\gamma/2$ in shallow water and to the local steepness $S = kH/2$ in deep water. Thus, F may be considered to be a unified nonlinearity parameter in arbitrary depth (Beji, 1995; Kirby, 1998). Further, using the results from linear theory, we can readily obtain $F = u_{\text{lin}}/c_{\text{lin}} = B_{\text{lin}}$, where u_{lin} is the linear theory prediction of the particle velocity at the horizontal crest position and at the mean water level. All of these properties suggest that F is a preferable diagnostic geometric parameter compared to γ and S for a unified breaking onset criterion in arbitrary depth.

We define a wave front slope θ in degrees by

$$\theta = \frac{180}{\pi}\tan^{-1}(H_c/l_1), \tag{15}$$

where H_c/l_1 is the crest front steepness (see Figure A1). We further define $\mathcal{A}_v = H_c/H$ and $\mathcal{A}_h = l_1/l_2 - 1$, which represent instantaneous vertical and horizontal asymmetry of the evolving crest and are related to the statistical third-order moments, normalized wave skewness $\overline{\eta^3}/\overline{\eta^2}^{3/2}$ and asymmetry $\overline{\mathcal{H}(\eta)^3}/\overline{\eta^2}^{3/2}$ (where $\mathcal{H}$ denotes the Hilbert transform), respectively. Finally, we define $\mathcal{A}_h' = l_1'/l_2' - 1$, which represents the horizontal asymmetry of the shape of the crest but only considering the upper half part of the crest. $\mathcal{A}_h'$ is also applicable for crests without zero-crossing points and is a more robust measure compared to $\mathcal{A}_h$ for crests with noticeable irregularity at their back face (Figure A2b).

The parameter θ is often used as the diagnostic criterion for the onset of breaking in Boussinesq models using eddy viscosity-type dissipation to model breaking (see, e.g., Kennedy et al., 2000; Schäffer et al., 1993). A maximum value of θ has also been used as a breaking criterion in potential flow models. Thus, in their 2-D-FNPF-BEM model, Guignard and Grilli (2001) used a maximum slope criterion to trigger dissipation using an "absorbing surface pressure." Grilli et al. (2019) revised and extended this earlier work
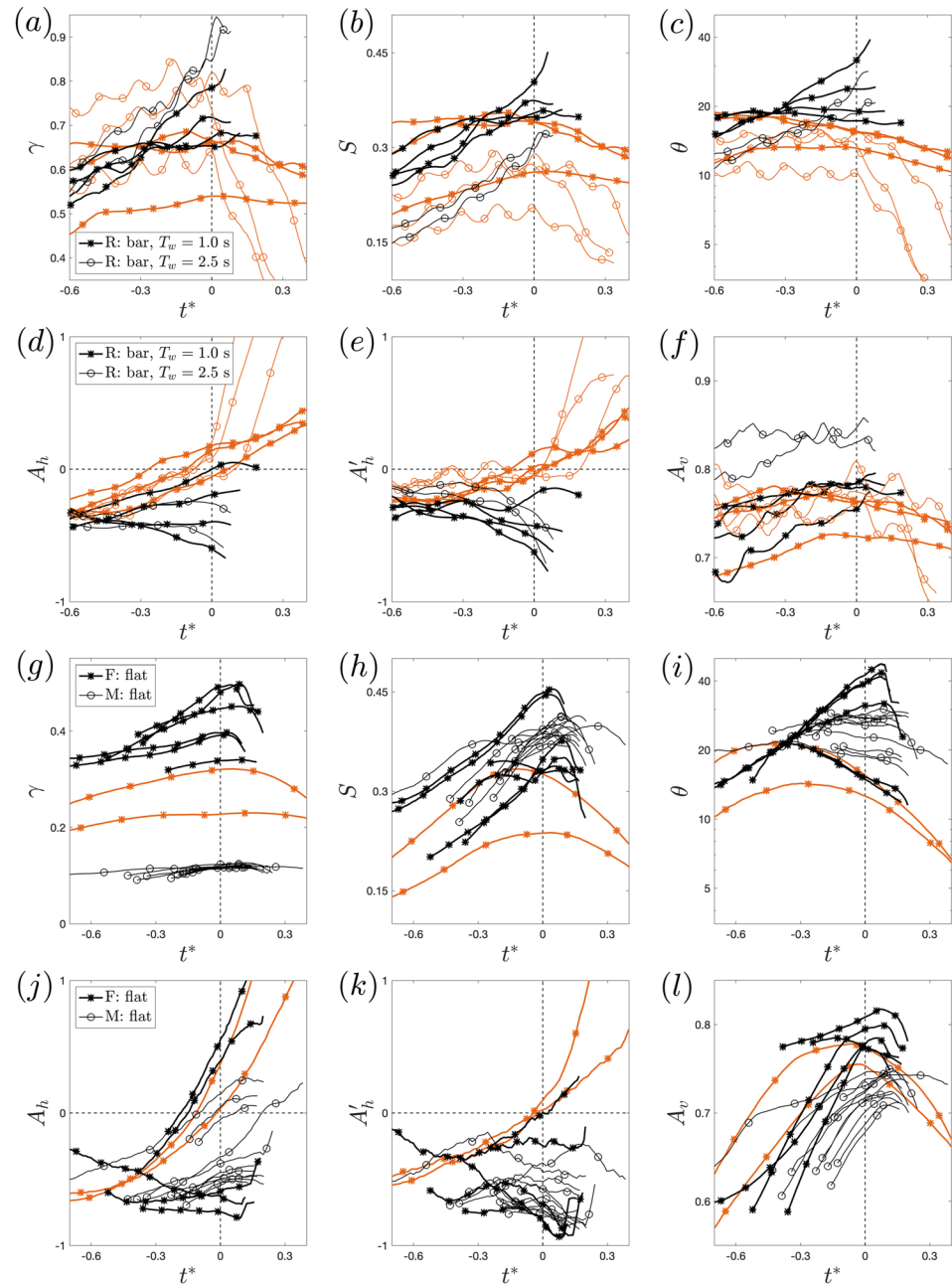
Figure 9. Examples of temporal evolution of various geometric parameters defined in section 5.1 (also see Figure A1) for breaking (black lines and symbols) and nonbreaking (orange lines and symbols) wave crests (a–f) in shallow water, and (g–l) in intermediate depth and deep water. The capital letters in the legend indicate the type of incident waves, R: regular waves, F: focused packets, and M: modulated wave trains. In the legend, bar and flat denote bar geometry (Figure 1b) and flat bed (Figure 1c), respectively, and T_w is the period of the regular incident waves.

and Papoutsellis et al. (2019) implemented and tested a similar criterion and energy absorption method in their 2-D-FNPF model. Finally, Mivehchi (2018) used a combination of maximum front slope and crest curvature as a breaking criterion in his 3-D-BEM model. Note that in such energy conserving models, the energy of breaking waves is dissipated by applying an "absorbing" surface pressure specified opposite and proportional to the free surface velocity or similar.
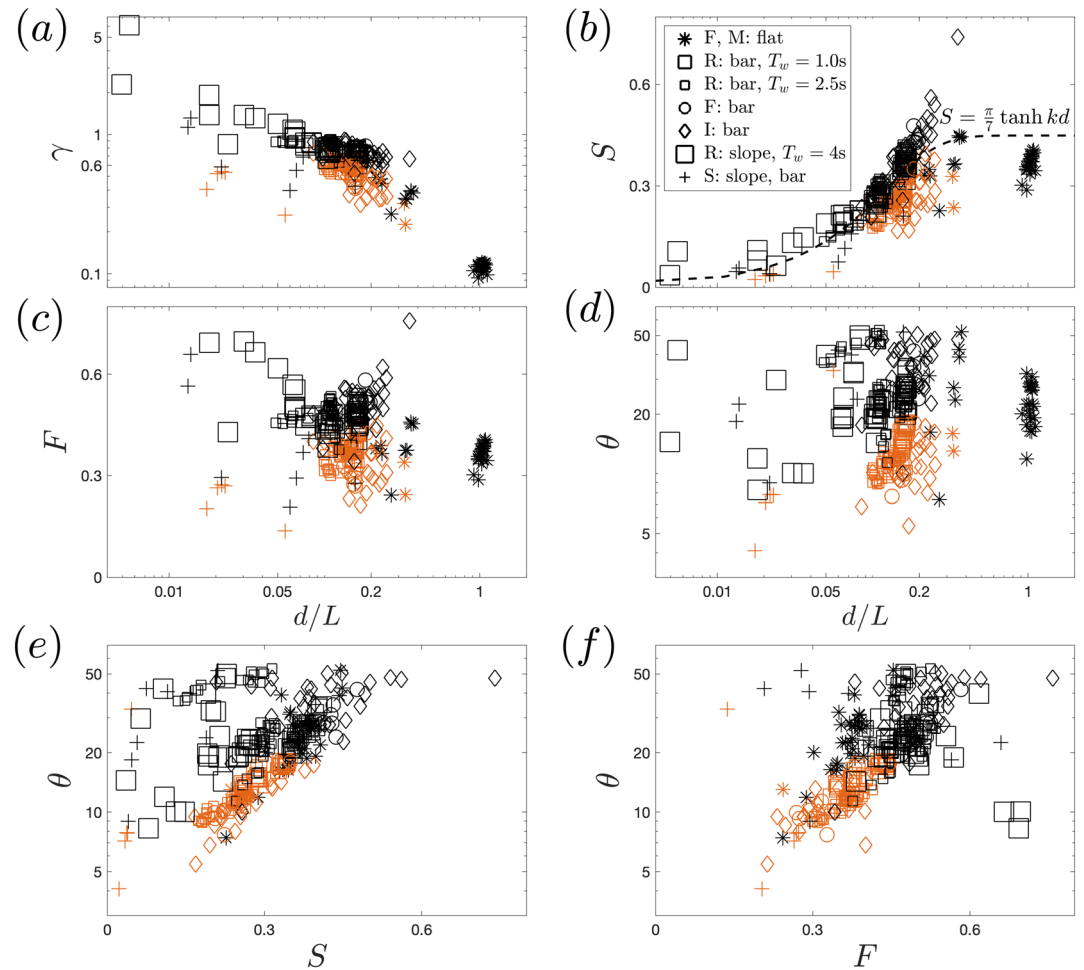
Figure 10. Variation of various geometric parameters, defined in section 5.1, at the breaking inception time or crest maximum, for all simulated breaking (black symbols) and nonbreaking (orange symbols) wave crests from deep to shallow water. The capital letters in the legend refer to the type of incident waves, R: regular, I: irregular, S: solitary waves, F: focused packets, and M: modulated wave trains. Here, $\gamma = H/d$ is the nonlinear parameter (or breaking index), $S = \pi H/L$ is the wave steepness, $\theta = 180/\pi\tan^{-1}(H_c/l_1)$ is the wave front slope (all are defined in Figure A1), and $F = ga/c_{\text{lin}}^2$ is the wave Froude number.

5.2. Evaluation of Predictive Skills of Existing Geometric Breaking Criteria

Figure 9 shows examples of computed temporal variation of the various geometric parameters defined in section 5.1 (also in Figure A1) for breaking (black lines and symbols) and nonbreaking (orange lines and symbols) wave crests from shallow to deep water. Examples shown in frames (a–f) represent regular waves shoaling over a submerged bar with a front face slope of 1/20 (Figure 1b), in which breaking is typically observed over the flat region of the bar and is characterized as shallow breaking. Examples shown in frames (g–l) represent focused packets and modulated waves propagating in intermediate and deep water over constant depth. Further, Figure 10 shows variation of the four geometric parameters γ, S, F and θ (section 5.1) at the time when $B = 0.85$ or at the unbroken crest maximum, for which $t^* = 0$, for all simulated breaking (black symbols) and nonbreaking (orange symbols) wave crests from shallow to deep water (which includes cases shown in Figure 9).

The most commonly used breaking onset parameter in shallow water wave breaking is $\gamma = H/d$; in phase-averaged models the mean depth $d + \bar{\eta}$ is typically used instead of still water depth d, such that mean wave setup or setdown is included. There is a large body of literature including laboratory and field studies attempting to define γ values at breaking onset for various incident waves in shallow water. An extensive review is given in Robertson et al. (2013). Observed values of γ at breaking onset, in a wave-by-wave sense, are typically greater than 0.6 in shallow water. Consistent with the existing relevant literature, results shown

in Figures 9a and 9g indicate that γ increases as a wave approaches the breakpoint and that γ at breaking onset is an increasing function of the surf-similarity parameter ξ_0 (Battjes, 1974; Raubenheimer et al., 1996). However, no unified formulation of γ predicting the onset of depth-limited wave breaking can be found (see Figure 10a). Further, it is clear that γ is an irrelevant parameter for estimating the breaking onset of steepness-limited wave breaking in deep water.

In the shallow breaking cases shown in Figure 9a, the local depth d decreases over the front face of the bar (the shoaling region), then becomes constant over the top of the bar, and then increases over the back face of the bar (Figure 1b). The latter explains the noticeable decrease of γ for $t^* > 0$ for nonbreaking crests. During the time a nonbreaking crest propagates over the top of the bar (constant depth region) the variation of γ is relatively small.

Figures 9b and 9h indicate that as a crest approaches breaking, or its maximum height for nonbreaking crests, the local steepness $S = kH/2$ increases both in shallow and deep water cases. We observe that the maximum steepness values of all the simulated nonbreaking crests are smaller than that given by the Miche (1944) breaking steepness criterion $S = \pi/7 \tanh kd$ (dashed line in Figure 10b). We also observe that a large number of simulated breaking crests occur with a steepness value smaller than the limiting criterion. We note that our definition of L is different from the classical definition for wavelength; our L is much smaller than the latter in some of the shallow breaking cases considered here (see Appendix A). In summary, breaking is clearly related to steepness, but a unified formulation that is able to predict maximum values of S at breaking onset from deep to shallow water remains unknown; the same conclusion holds for the wave Froude number F (Equation 14) (Figure 10c).

Figures 9c and 9i as well as Figure 10d document the variation of the wave front slope θ (Equation 15) as a function of time and at $t^* = 0$, respectively, from shallow to deep water. In general, breaking crests have higher maximum values of θ compared to nonbreaking crests. However, most of the spilling breakers, both in deep and shallow water, maintain their maximum θ values as they approach the breakpoint. Moreover, θ decreases slightly as a crest approaches breaking in marginal breaking cases, both in deep and shallow water. These observations suggest that θ might be a useful diagnostic breaking onset parameter but should be combined with other parameters; such as γ in shallow and with S (shown in Figure 10e) in deep water or, more generally, with the wave Froude number F (shown in Figure 10f) in order to potentially predict the breaking onset time and location in a phase resolved sense.

Finally, Figures 9d–9f and 9j–9l demonstrate that neither the horizontal ($\mathcal{A}_h$ and $\mathcal{A}_h'$) nor the vertical asymmetry of an evolving crest (as defined in section 5.1) are a good candidate as a breaking onset parameter. Further, results show that some of the simulated wave crests, both in shallow and deep water, are remarkably symmetric just prior to breaking ($\mathcal{A}_h \approx 0$). This result is consistent with field observations made using stereo photography in deep water (Schwendeman & Thomson, 2017) and with field observations using LIDAR in shallow water (Carini, 2018).

In summary, our results reveal that a criterion using both θ and F has relatively higher skill in predicting the onset of breaking from deep to shallow water, compared to the other geometric parameters considered here. However, such a criterion still cannot segregate all breaking crests from nonbreaking ones.

5.3. Two- Versus Three-Dimensional Shoaling and Breaking Waves

While, in shallow water, most breakers end up being locally nearly 2-D, 3-D processes of directional and bathymetric focusing can affect or even govern the evolution of shoaling waves toward breaking. Earlier work with 2-D- and 3-D-BEM models, however, indicates that whether in 2-D (Grilli et al., 1997) or 3-D (Guyenne & Grilli, 2006) once a wave approaches breaking onset, there is a "loss of memory" of the physical phenomenon(a) that have led to breaking and whether a crest breaks or not and how it breaks essentially depends on local wave properties (here represented by U and C at the crest). Guyenne and Grilli (2006), for instance, compared properties of solitary waves shoaling over a 3-D sloping ridge or a 2-D plane slope in their 3-D-BEM model and found similar velocity and acceleration fields near the crest and in the jet of breaking waves. This supports the present investigation of 2-D shoaling and breaking waves in shallow water. Nevertheless, in future work, we will consider more complex shallow water bathymetries and confirm the validity of the breaking inception threshold value $B_{th} \approx 0.85$ for breaking wave crests in such more realistic 3-D shoaling cases.

5.4. Implementation of the Parameter B in Energy-Conserving Phase-Resolving Models

The new criterion is suitable for use in wave-resolving models that cannot intrinsically detect the onset of wave breaking. Some of these models, such as High Order Spectral (HOS) models (Dommermuth & Yue, 1987; West et al., 1987), become unstable if they reach the visible breaking onset stage, that is, $B = 1$. Thus, warning of imminent breaking onset at $B_{th} \approx 0.85$ is critical in the context of the successful application of the new criterion in such wave-resolving energy-conserving models; because at $B = B_{th}$ the waveform is well defined, no vertical tangent occurs on the wave front face, and the free surface is single-valued.

In a practical implementation of the B_{th} criterion in wave models such as HOS or Boussinesq, one would be able to track the evolution of $B = U/C$ up to the point where the criterion is verified, provided wave crests can be identified. This was already demonstrated for simple 2-D shoaling solitary waves, for instance, by Wei et al. (1995) using a fully nonlinear Boussinesq model and by Seiffert and Ducrozet (2018) for HOS. While a crest location and its velocity C can be easily computed in these 2-D models, this is more difficult to do in 3-D. Stansell and MacFarlane (2002) identified crests in experimental results and computed their velocity c based on a Hilbert transform of the free surface. This method was applied by Mivehchi (2018) to detect wave crests and compute their velocity in results of a 3-D-BEM model, and suppress breaking waves by specifying an "absorbing surface pressure"; here breaking was based on a maximum crest curvature/front-slope criterion. A similar Hilbert-transform-based method could be applied to detect crests and compute their celerity in results of (2-D horizontal) HOS or Boussinesq models. In the Boussinesq model, the particle velocity at the crest would be obtained from extrapolating to the surface the horizontal velocity used in the model at some predefined depth, using the model's assumed velocity profile (e.g., parabolic). This could be facilitated by formulating the Boussinesq model with a vertical boundary-fitted σ coordinate (as recently proposed by Kirby, 2020), which enables the simple projection of the model horizontal velocity to $\sigma = 1$.
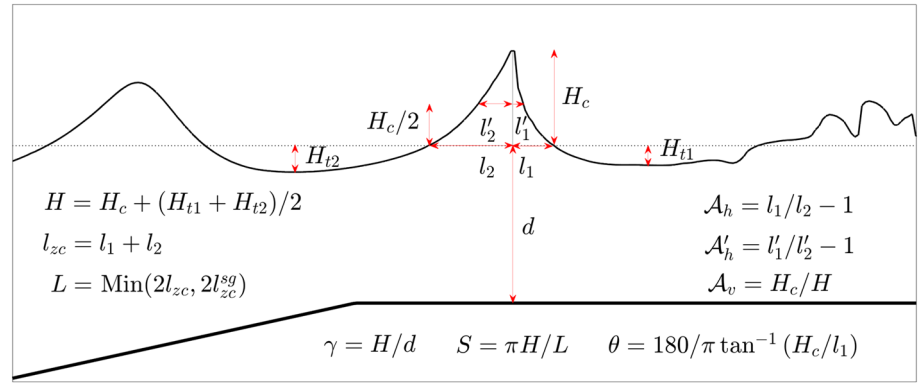
6. Conclusions

The model simulation results presented here extend the results of B18 to cases of waves shoaling and breaking in shallow water. The local energy flux parameter B exceeding the threshold of ≈ 0.85 is confirmed to provide a robust predictor of breaking onset for cases where breaking results from a crest instability. In particular, we have simulated cases where a weak modulation of periodic waves by tank seiching leads to occasional breaking events in a train of otherwise unbroken waves, which are marginally close to breaking. These breaking events are clearly indicated by the passage of B through the ≈ 0.85 threshold. Further, we have shown that $B_{th} \approx 0.85$ clearly separates breaking and nonbreaking cases for shoaling/deshoaling waves propagating over bars. We conclude that this investigation provides further support for the generic applicability of the new breaking framework proposed by B18, which was developed with specific reference to the onset of instability and incipient overturning in the region localized around wave crests.

Our extension to shoaling waves introduces the additional phenomenon of surging breakers, with breakdown and generation of turbulence during the uprush of a surging wave on a beach. This may be related more directly to instabilities of the strongly curved flow closer to the toe of the surging wave front. This process is very different in nature from the mechanism covered by the analysis of B18 and occurs without a crest-based criterion being exceeded. It thus represents a different route to breaking whose occurrence (or onset) would require an alternate criterion to be developed.

We emphasize that the validity of the proposed criterion also needs to be examined in the presence of wind forcing. The laboratory work of Saket et al. (2018) showed that $B_{th} \approx 0.85$ also segregates breaking from nonbreaking crests in the presence of wind forcing in deep water breaking. A number of high-fidelity two-phase flow simulations of breaking waves in the presence of wind forcing (e.g., Tang et al., 2017; Yang et al., 2018) have been recently performed. Detailed quantification of the effect of direct wind forcing on the proposed breaking onset criterion in shallow water is left for future study.

Appendix A: Sensitivity of Local Geometric Parameters Used in the Analysis

Definitions of the various local geometric parameters for an evolving wave crest are described in Figure A1. Among these, the height H and length L of the carrier wave need to be defined first. Two main sources of uncertainty in the value of the geometric parameters defined in section 5.1 are the selected definitions of the local length L and height H of an evolving crest. Here we quantify such uncertainties in detail. In summary,

$$H = H_c + (H_{t1} + H_{t2})/2$$
$$l_{zc} = l_1 + l_2$$
$$L = \mathrm{Min}(2l_{zc}, 2l_{zc}^{sg})$$

$$\mathcal{A}_h = l_1/l_2 - 1$$
$$\mathcal{A}'_h = l'_1/l'_2 - 1$$
$$\mathcal{A}_v = H_c/H$$

$$\gamma = H/d \qquad S = \pi H/L \qquad \theta = 180/\pi \tan^{-1}(H_c/l_1)$$

Figure A1. Local geometric parameters describing an evolving wave crest. Here l_{zc}^{sg} represents a length scale obtained from a skewed-Gaussian fit to the crest region. Dotted and thick solid lines show the still water and the bed elevations, respectively. The incident waves are propagating from left to right.

using definitions other than those used here may vary the estimated H values for extreme waves by up to 10%. However, the sensitivity of the estimated L values at breaking onset are noticeably larger, especially for shallow cases.

Following Derakhti and Kirby (2016), D18, and Tian et al. (2008), we define the local wave length $L = 2l_{zc}$, where $l_{zc} = l_1 + l_2$ (Figure A1) is the distance between the two consecutive zero-crossing points adjacent to the crest. We note that the zero-crossing point on the back face of the wave may have noticeably large fluctuations due to the presence of higher harmonics in shallow water cases (Figure A2b) or high-frequency components in random waves, and so forth. Further, in some shallow water cases, for example, solitary waves, there are no zero-crossing points and thus l_{zc} can not be defined.

To resolve these issues, we fit a skewed-Gaussian function to the instantaneous wave profile and then estimate a length scale l_{zc}^{sg} from the skewed-Gaussian fitting as described below (Figure A2). Finally, we take $L = \mathrm{Min}(2l_{zc}, 2l_{zc}^{\mathrm{sg}})$ as the local wave length.
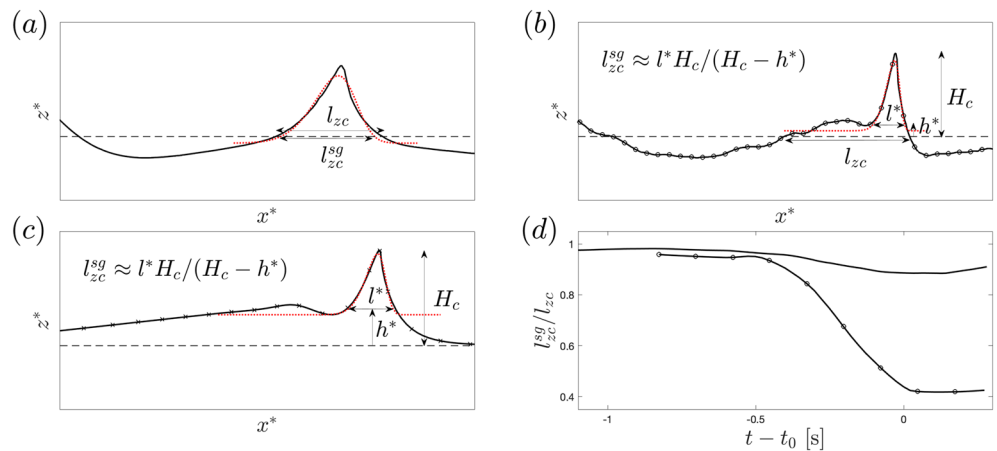
Figure A2. (a, b, c) Definition of the local zero-crossing length-scale l_{zc}^{sg} obtained from skewed-Gaussian fitting (dotted lines) to the wave profile (solid lines) for examples of evolving crests shoaling over a submerged bar as well as (d) the temporal variation of $l_{zc}^{\mathrm{sg}}/l_{zc}$ before (shoaling phase) and after the breaking onset ($t = t_0$) for the crests shown in (a) and (b). (a) Regular waves with $T_w = 1.01$ s, (b) regular waves with $T_w = 2.525$ s, and (c) a solitary wave. Note that l_{zc} does not exist for solitary waves. In (a–c), the dashed lines show the still water levels.
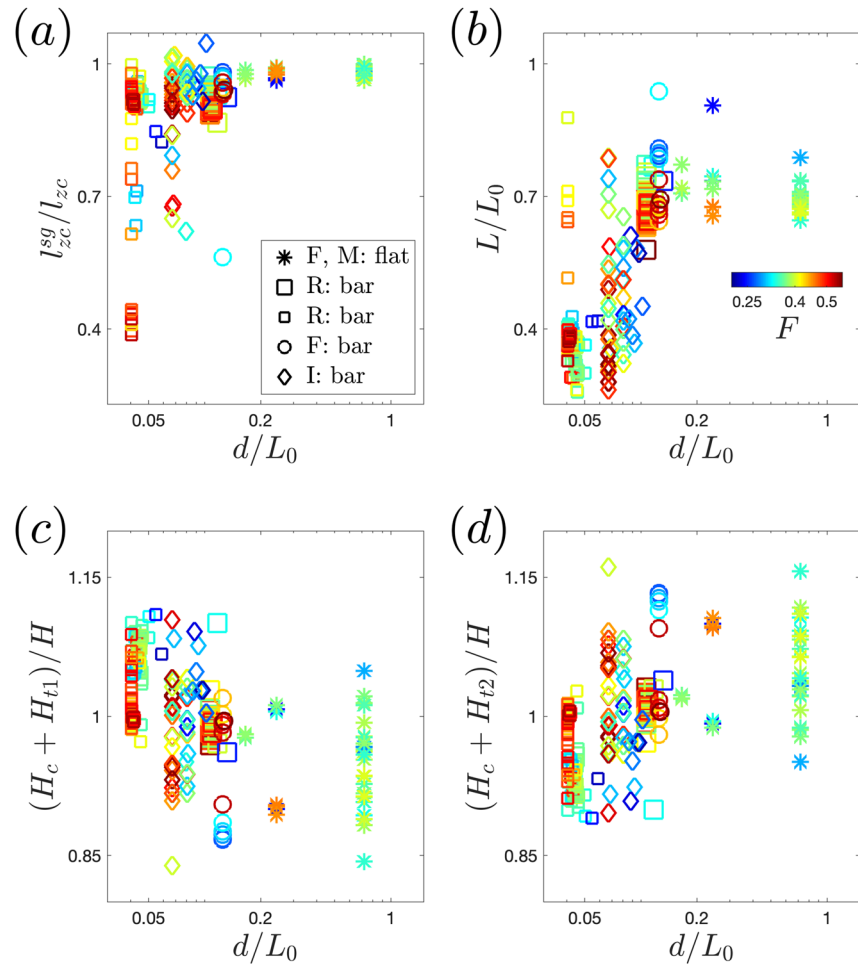
Figure A3. Sensitivity of the local height and length of an evolving crest from deep to shallow water. (a) the ratio between the length scales l_{zc}^{sg} obtained from skewed-Gaussian fitting defined in Equation A1 and l_{zc} both shown in Figure A2; and (b) the ratio between the zero-crossing length scale $L = \text{Min}(2l_{zc}, 2l_{zc}^{sg})$ and a wave length L_0 at breaking onset for the breaking crests or at the time at which $H_c = \eta_{\max}$ for the nonbreaking crests. Here, L_0 is obtained by using the linear dispersion relation $(2\pi/T_0)^2 = gk_0 \tanh[k_0 d]$ with d the still water depth, $k_0 = 2\pi/L_0$ and T_0 equals to paddle period for monochromatic waves and peak period T_p for incident irregular waves.

Here l_{zc}^{sg} is a length scale obtained from the skewed-Gaussian fit $f(r)$ defined as a scaled product of the standard normal probability density function $\varphi(r) = \exp[-r^2/2]/\sqrt{2\pi}$ and its cumulative distribution function $\Phi(r) = (1 + \text{erf}[r/\sqrt{2}])/2$ (erf denotes the error function) given by

$$f(r) = c_1 \varphi(r) \Phi(\alpha r) + c_2, \tag{A1}$$

where $r = (x - x_p)/\omega$ with x_p and ω are the peak location and scale, respectively, α the horizontal skewness parameter ($\alpha < 0$ for waves pitch forward), c_1 a scaling parameter and c_2 a vertical offset. The instantaneous f for each crest is obtained by a nonlinear fitting of Equation A1, including five coefficients, to the corresponding simulated wave profile.

Figures A2a–A2c show examples of f (dotted lines) and the corresponding l_{zc}^{sg}, just before breaking onset time, for three simulated evolving crests shoaling over a submerged bar. In addition, Figure A2d shows the temporal variation of the ratio l_{zc}^{sg}/l_{zc} for the two examples shown in frames (a) and (b). Frames (b) and (d) show that we may have $l_{zc}^{sg} \ll l_{zc}$ at breaking onset in cases with irregularities on the back face of the wave, for example, due to the presence of higher harmonics. Finally, in solitary cases (Figure A2c) we simply define $L = 2l_{zc}^{sg}$ because there are no zero-crossing points and thus l_{zc} cannot be defined.

At breaking onset, Figure A3a demonstrates that the length scale l_{zc}^{sg} obtained from the skewed Gaussian fitting (Equation A1) is usually smaller than the zero-crossing length scale l_{zc} (Figure A2). Our results show

that $l_{zc}^{sg}/l_{zc} > 0.9$ in most cases, especially for those with $d/L_0 > 0.1$, with d the still water depth and L_0 a prediction of the local wave length obtained by using the linear dispersion relation $(2\pi/T_0)^2 = gk_0\tanh[k_0 d]$ with $k_0 = 2\pi/L_0$ and T_0 equal to paddle period for monochromatic waves and peak period T_p for incident irregular waves. In some of the shallow cases ($d/L_0 < 0.1$), however, we observe l_{zc}^{sg}/l_{zc} values down to 0.4. Figure A3b shows that our definition of L represents a smaller length scale compared to the characteristic wave length L_0 where the averaged values of L vary between $L_0/3$ in shallow water up to $0.7L_0$ in intermediate and deep water.

We define the local wave height H as the sum of a crest elevation and averaged trough elevations before and after the crest, $H = H_c + (H_{t1} + H_{t2})/2$. Our results (Figures A3c and A3d) indicate that other potential definitions of wave height such as $H_c + H_{t1}$ or $H_c + H_{t2}$ are within 10% of $H = H_c + (H_{t1} + H_{t1})/2$ in most cases from deep to shallow water. In addition, the downstream trough height H_{t1} is greater than or equal to the upstream trough height H_{t2} in shallow water cases; the trend is reversed in deep water cases. These trough heights vary between $0.2H_c$ and $0.5H_c$ in most cases.

Appendix B: Model Validation for Shallow Water Breaking

In this section, the validation of the LES/VOF model (Derakhti & Kirby, 2014a) including detailed comparisons of free surface evolution and organized and turbulent velocity fields, is presented for a number of available laboratory data for breaking and nonbreaking waves in shallow water. The reader is referred to Derakhti and Kirby (2014a, 2014b, 2016) for the detailed examination of the model prediction of the free surface evolution, organized and turbulent velocity fields, bubble void fraction, integral properties of the bubble plume, and the total energy dissipation compared with corresponding measured data, as well as the sensitivity of the simulation results with respect to the selected grid resolution for focusing laboratory-scale breaking packets in intermediate depth and deep water.

In all the simulated cases using the LES/VOF model, the selected horizontal grid size in the wave propagation direction (which is always $+x$ direction here) Δx is smaller than 1/100 of the dominant wavelength at the x location at which the crest maximum was observed, and $\Delta z = \Delta y \leq \Delta x$. Using such spatial resolution, our LES/VOF model captures the free surface and organized velocity field fairly accurately up to the break point, and the estimates of the loss of total wave energy due to wave breaking are typically within 10% of observed levels (Derakhti et al., 2018; Derakhti & Kirby, 2014a), after correcting for the change in the downstream group velocity following breaking in isolated breaking waves (Derakhti & Kirby, 2016).

Regarding the FNPF-BEM model used in this work, Grilli et al. (1994) showed that surface elevations simulated with the model for solitary waves shoaling over plane slopes agreed within 1–2% with measured surface elevations, up to the breaking point. Grilli et al. (1994) reported a similarly good agreement of numerical results with experiments for solitary waves propagating over a trapezoidal breakwater. Grilli et al. (1997) showed that the model could accurately predict breaking crest elevations, breaker index, and breaker types for solitary waves of various incident height propagating over mild to steep slopes. Finally, Grilli et al. (2019) show that the model also accurately simulates the shoaling and propagation of periodic waves over a bar similar to that considered here.

Table B1
Input Parameters for the Simulated Cases Used for the Validation of the LES/VOF Model

Case	H_w (mm)	T_w (s)	d_1 (m)	L_1 (m)	s	ξ_0	d_2 (m)	L_2 (m)	s_d	Exp.
P10-r	122	2.0	0.36	0	$\frac{100}{3}$	0.21	–	–	–	Ting and Nelson (2011)
	125	2.0	0.4	0	35	0.20	–	–	–	Ting and Kirby (1994)
B1-r	41.0	1.01	0.4	6	20	0.30	0.1	2	10	Luth et al. (1994)
B3-r	29.0	2.53	0.4	6	20	0.95	0.1	2	10	Luth et al. (1994)
B9-r	97.2	1.43	0.7	2	10	0.57	0.08	0	0	Blenkinsopp and Chaplin (2007)

*Note.* Definitions are given in Table 1.
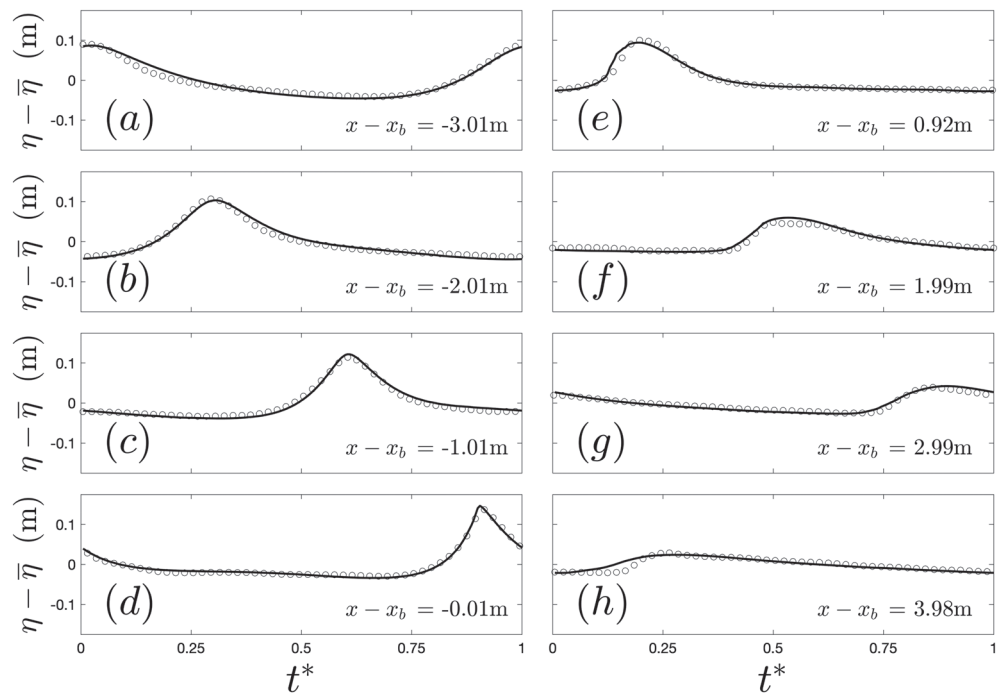
Figure B1. Comparison between the LES/VOF model results of spanwise-phase-averaged free surface elevations at various cross-shore locations for the case P10-r and the corresponding measurements by Ting and Nelson (2011). No spanwise averaging was involved in the measurement.

B1. Regular Waves Shoaling Over a Plane Beach

Here we consider the LES/VOF model performance for the case of regular depth-limited wave breaking on a planar beach (P10-r) in terms of phase-averaged free surface elevations and wave height using the data set of Ting and Nelson (2011). We also compare the model results of the case P10-r with the free surface and velocity measurements of the spilling case of Ting and Kirby (1994). The experimental setup and incident wave conditions of the latter are similar as in P10-r and are also summarized in Table B1. This experiment has been widely used by other researchers to validate both RANS (Derakhti et al., 2015, 2016a, 2016b, 2016c; Lin & Liu, 1999; Ma et al., 2011) and LES (Christensen, 2006; Lakehal & Liovic, 2011) numerical models.

Figure B1 shows that the model captures the evolution of phase-averaged free surface elevations reasonably well compared with the corresponding measurements of Ting and Nelson (2011) in the shoaling, transition and inner surfzone. Further, Figure B2 shows the comparison between the predicted and observedcross-shore variation of the wave height H calculated from the phase-averaged free surface time-series. Here phase averaging is performed over N successive waves after the wave field reaches a steady state condition, where N is 10 in both the simulated results and the measurements.
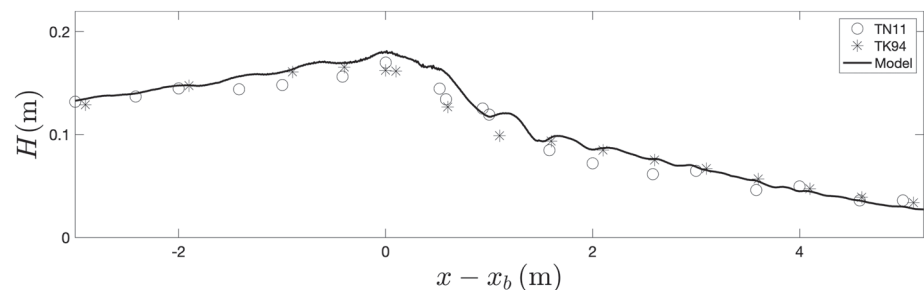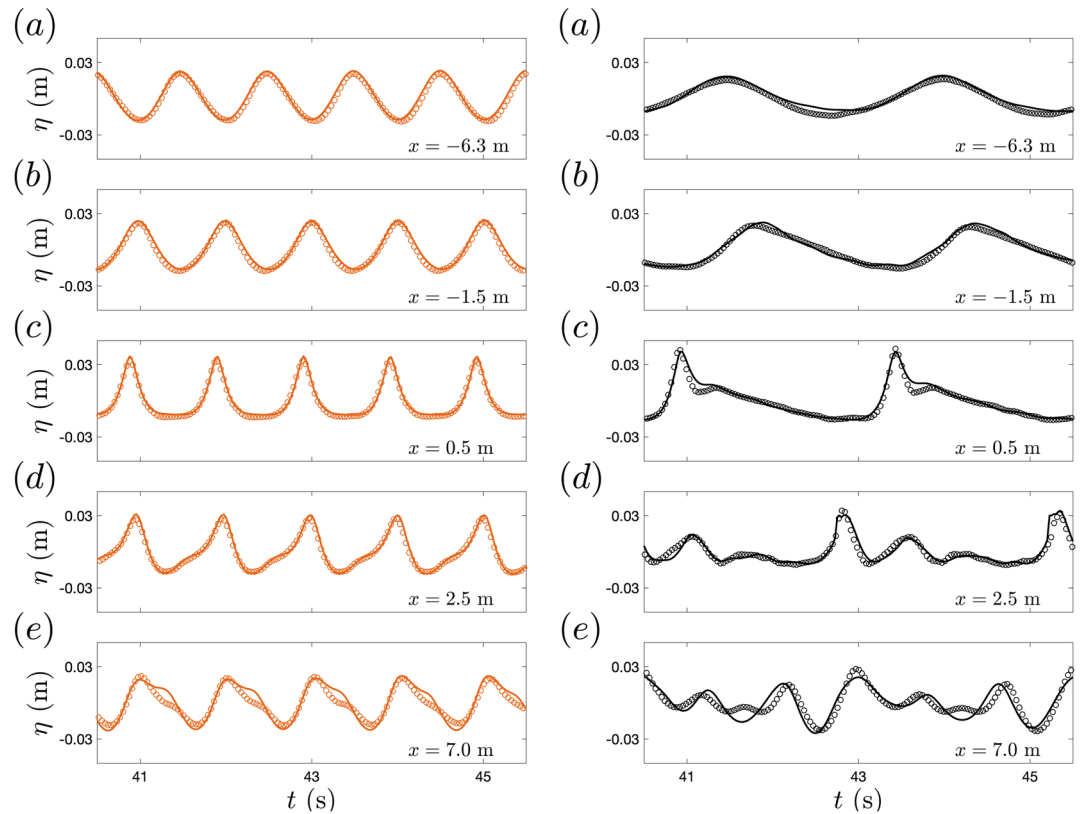

Figure B2. The LES/VOF model-data comparison of the cross-shore variation of the wave height H for the case P10-r. Here TN11 and TK94 denote the data set of Ting and Nelson (2011) and Ting and Kirby (1994), respectively.
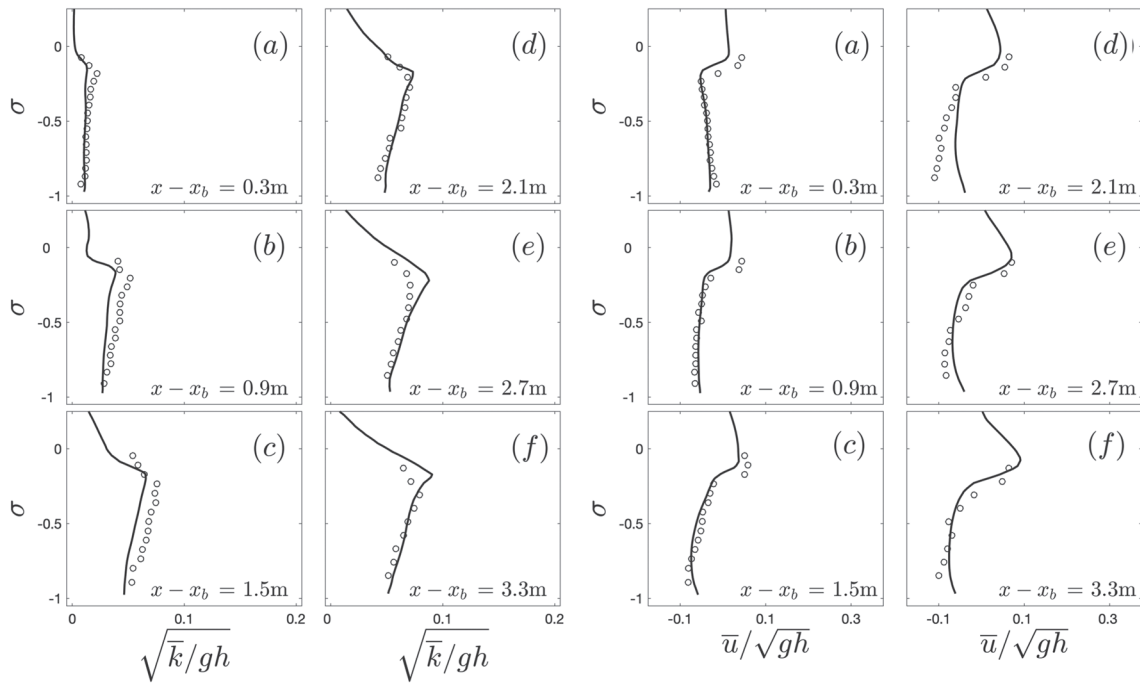
Figure B3. The LES/VOF model results of spanwise-time-averaged normalized (a–f) turbulent kinetic energy, $\sqrt{\overline{k}/gh}$, and (A–F) horizontal velocity, $\overline{u}/\sqrt{gh}$, (undertow) profiles for the case P10-r at various cross-shore locations after the initial break point. Circles show the measurements of Ting and Kirby (1994). Here, $\sigma = (z - \overline{\eta})/h$ and $h = d + \overline{\eta}$.

Figure B4. Comparison of the LES/VOF model results (solid lines) and measurements (Luth et al., 1994) (circles) of free surface elevations at various x locations for the along-crest uniform (a–e) nonbreaking, with $T_w = 1.01$ s and $H_w = 0.041$ m, and (A–E) breaking, with $T_w = 2.525$ s and $H_w = 0.029$ m, regular waves shoaling over a submerged bar. Here $-6 < x < 0$ and $0 < x < 2$ indicate the up-slope and top of the bar, respectively (see Figure 1c and Table B1).
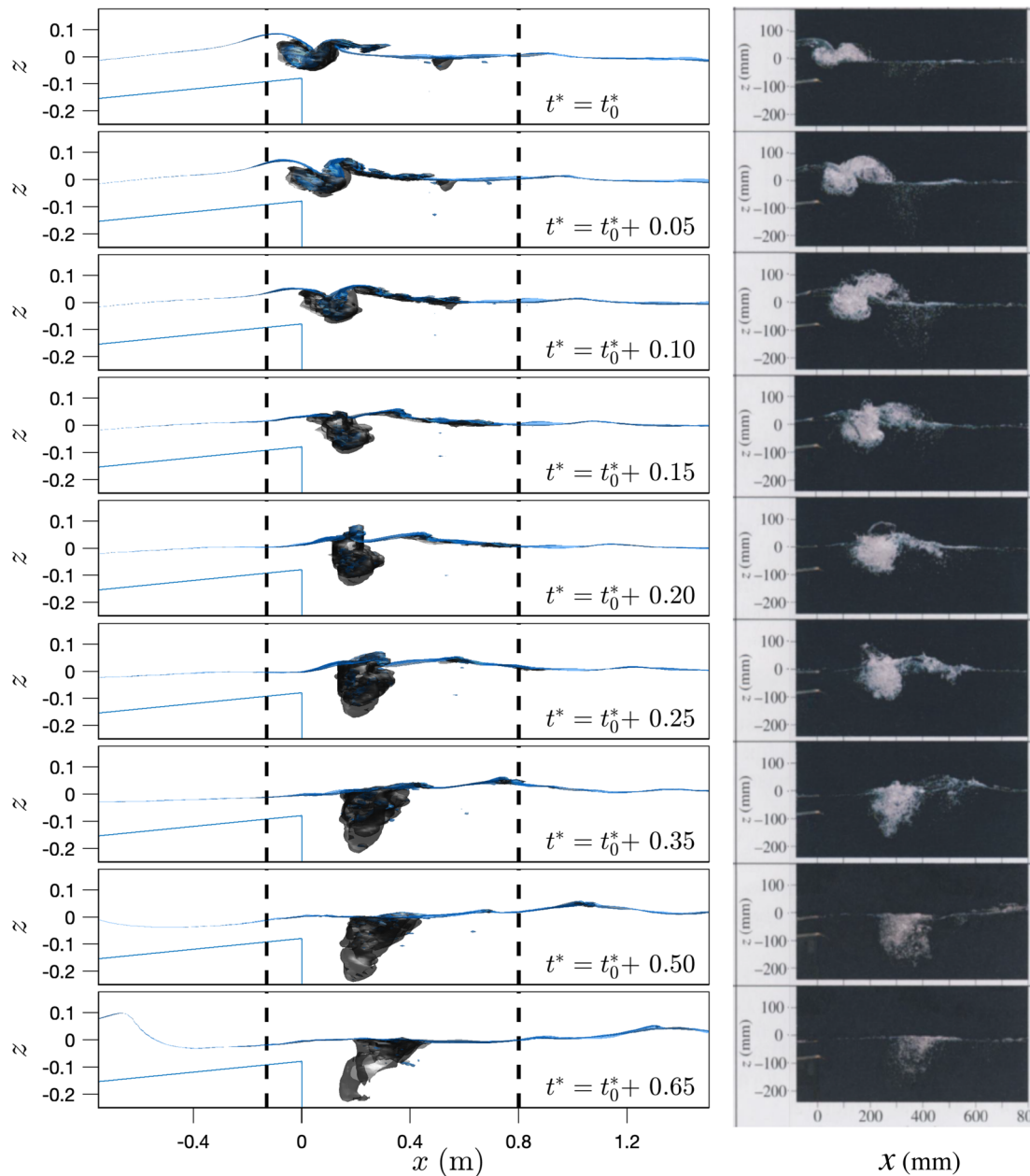
Figure B5. Comparison of the side view of the predicted (left column) and observed (right column) bubble plume evolution for the case B9-r. The two dashed lines in the right column indicate the field of view of the photographs, adopted from Blenkinsopp and Chaplin (2007, Figure 4).

Figure B2 also shows that the spatial evolution of H relative to the break point in the case P10-r is comparable with that in the spilling case of Ting and Kirby (1994). Thus, although the incident wave conditions and setup in the latter are slightly different than those in the case P10-r the wave-driven currents and turbulence statistics should be comparable.

Figure B3 shows the spatial distribution of the normalized spanwise-time-averaged, turbulent kinetic energy, and horizontal velocity, for the case P10-r. Figure B3 shows that both the magnitude and spatial variation of the predicted $\overline{\langle k \rangle}^{1/2}/\sqrt{gh}$ and $\overline{\langle u \rangle}/\sqrt{gh}$ are consistent with the corresponding measured values of Ting and Kirby (1994) in the transition and inner surf zone.

B2. Regular Waves Shoaling Over an Idealized Bar

Here we consider the LES/VOF model performance for cases of regular nonbreaking (B1-r) and breaking (B3-r and B9-r) waves shoaling over a submerged bar, using the data sets of Luth et al. (1994) and

Blenkinsopp and Chaplin (2007). Figures B4 and B5 document that the model accurately captures the non-linear evolution of evolving crests propagating over the up-slope $(-s(d_1 - d_2) < x < 0)$ and top $(0 < x < L_2)$ of the bar in all cases. Figure B5 also shows that the model fairly reasonably predicts the kinematics of the entrained bubble plume compared to the observations. The apparent mismatch between the predicted and observed wave profiles is mainly due to the mismatch between their corresponding incident waves and due to the difference between the low-frequency wave climate in the numerical and laboratory wave tanks.

References

Babanin, A., Chalikov, D., Young, I., & Savelyev, I. (2007). Predicting the breaking onset of surface water waves. *Geophysical research letters*, *34*, L07605. https://doi.org/10.1029/2006GL029135

Banner, M., Barthelemy, X., Fedele, F., Allis, M., Benetazzo, A., Dias, F., & Peirson, W. (2014). Linking reduced breaking crest speeds to unsteady nonlinear water wave group behavior. *Physical Review Letters*, *112*(11), 114,502.

Banner, M. L., & Peirson, W. L. (2007). Wave breaking onset and strength for two-dimensional deep-water wave groups. *Journal of Fluid Mechanics*, *585*, 93–115.

Banner, M. L., & Peregrine, D. H. (1993). Wave breaking in deep water. *Annual Review Fluid Mechanics*, *25*, 373–397.

Barthelemy, X., Banner, M. L., Peirson, W. L., Fedele, F., Allis, M., & Dias, F. (2018). On a unified breaking onset threshold for gravity waves in deep and intermediate depth water. *Journal of Fluid Mechanics*, *841*, 463–488.

Battjes, J. A. (1974). Surf similarity. In *Proceedings of the 14th International Conference on Coastal Engineering* (pp. 466–480). Copenhagen, Denmark: ASCE.

Beji, S (1995). Note on a nonlinearity parameter of surface waves. *Coastal Engineering*, *25*, 81–85.

Blenkinsopp, C. E., & Chaplin, J. R. (2007). Void fraction measurements in breaking waves. *Proceedings of the Royal Society A*, *463*, 3151–3170.

Booij, N. (1981). Gravity waves on water with non-uniform depth and current (Ph.D. Thesis), Technische Hogeschool, Delft (Netherlands).

Carini, R. J. (2018). Geometry, kinematics and energetics of surf zone waves near the onset of breaking using remote sensing (Ph.D. Thesis), University of Washington, Seattle, WA.

Carrica, P. M., Drew, D., Bonetto, F., & Lahey, R. T. (1999). A polydisperse model for bubbly two-phase flow around a surface ship. *International Journal of Multiphase Flow*, *25*, 257–305.

Christensen, E. D. (2006). Large eddy simulation of spilling and plunging breakers. *Coastal Engineering*, *53*, 463–485.

Craciunescu, C. C., & Christou, M. (2019). Identifying breaking waves from measured time traces. In *The 29th International Ocean and Polar Engineering Conference*, (pp. 2498–2505). Honolulu, Hawaii, USA.

Derakhti, M., Banner, M. L., & Kirby, J. T. (2018). Predicting the breaking strength of gravity water waves in deep and intermediate depth. *Journal of Fluid Mechanics*, *848*, R2.

Derakhti, M., & Kirby, J. T. (2014a). Bubble entrainment and liquid bubble interaction under unsteady breaking waves. *Journal of Fluid Mechanics*, *761*, 464–506.

Derakhti, M., & Kirby, J. T. (2014b). Bubble entrainment and liquid bubble interaction under unsteady breaking waves (*Research Report CACR-14-06*). Newark, Delaware: Center for Applied Coastal Research, Department of Civil and Environmental Engineering, University of Delaware. Available at http://www.udel.edu/kirby/papers/derakhti-kirby-cacr-14-06.pdf

Derakhti, M., & Kirby, J. T. (2016). Breaking-onset, energy and momentum flux in unsteady focused wave packets. *Journal of Fluid Mechanics*, *790*, 553–581.

Derakhti, M., Kirby, J. T., Shi, F., & Ma, G. (2015). NHWAVE: Model revisions and tests of wave breaking in shallow and deep water (*Tech. Rep. CACR-14-18*). Newark, Delaware: Center for Applied Coastal Research, Dept. of Civil & Environmental Engineering, University of Delaware.

Derakhti, M., Kirby, J. T., Shi, F., & Ma, G. (2016). NHWAVE: Consistent boundary conditions and turbulence modeling. *Ocean Modelling*, *106*, 121–130.

Derakhti, M., Kirby, J. T., Shi, F., & Ma, G. (2016). Wave breaking in the surf zone and deep-water in a non-hydrostatic RANS model. Part 1: Organized wave motions. *Ocean Modelling*, *107*, 125–138.

Derakhti, M., Kirby, J. T., Shi, F., & Ma, G. (2016). Wave breaking in the surf zone and deep-water in a non-hydrostatic RANS model. Part 2: Turbulence and mean circulation. *Ocean Modelling*, *107*, 139–150.

Dommermuth, D. G., & Yue, D. K. P. (1987). A high-order spectral method for the study of nonlinear gravity waves. *Journal of Fluid Mechanics*, *184*, 267–288.

Fedele, F., Chandre, C., & Farazmand, M. (2016). Kinematics of fluid particles on the sea surface: Hamiltonian theory. *Journal of Fluid Mechanics*, *801*, 260–288.

Francois, M. M., Cummins, S. J., Dendy, E. D., Kothe, D. B., Sicilian, J. M., & Williams, M. W. (2006). A balanced-force algorithm for continuous and sharp interfacial surface tension models within a volume tracking framework. *Journal of Computational Physics*, *213*, 141–173.

Grilli, S. T., Horrillo, J., & Guignard, S. (2019). Fully nonlinear potential flow simulations of wave shoaling over slopes: Spilling breaker model and integral wave properties. *Water Waves*, 1–35. https://doi.org/10.1007/s42286-019-00017-6

Grilli, S. T., Losada, M. A., & Martin, F. (1994). Characteristics of solitary wave breaking induced by breakwaters. *Journal of Waterway, Port, Coastal, and Ocean Engineering*, *120*(1), 74–92.

Grilli, S. T., Skourup, J., & Svendsen, I. A. (1989). An efficient boundary element method for nonlinear water waves. *Engineering Analysis with Boundary Elements*, *6*(2), 97–107.

Grilli, S. T., & Subramanya, R. (1996). Numerical modeling of wave breaking induced by fixed or moving boundaries. *Computational Mechanics*, *17*(6), 374–391.

Grilli, S. T., Subramanya, R., Svendsen, I. A., & Veeramony, J. (1994). Shoaling of solitary waves on plane beaches. *Journal of Waterway, Port, Coastal, and Ocean Engineering*, *120*(6), 609–628.

Grilli, S. T., Svendsen, I. A., & Subramanya, R. (1997). Breaking criterion and characteristics for solitary waves on slopes. *Journal of Waterway, Port, Coastal, and Ocean Engineering*, *123*(3), 102–112.

Guignard, S., & Grilli, S. T. (2001). Modeling of wave shoaling in a 2D-NWT using a spilling breaker model. In *The Eleventh International Offshore And Polar Engineering Conference*. Stavanger, Norway.

Guyenne, P, & Grilli, S. (2006). Numerical study of three-dimensional overturning waves in shallow water. *Journal of Fluid Mechanics*, *547*, 361–388.

Iribarren, C. R., & Nogales, C. (1949). Protection des ports. In *17th International Navigation Congress*, (Vol. *2*, pp. 31–80). Lisbon.

Kennedy, A. B., Chen, Q., Kirby, J. T., & Dalrymple, R. A. (2000). Boussinesq modeling of wave transformation, breaking and runup. I: 1D. *Journal of Waterway, Port, Coastal and Ocean Engineering*, *126*(1), 39–47.

Khait, A, & Shemer, L (2018). On the kinematic criterion for the inception of breaking in surface gravity waves: Fully nonlinear numerical simulations and experimental verification. *Physics of Fluids*, *30*(5), 57,103.

Kirby, J. T. (1998). Discussion of 'Note on a nonlinearity parameter of surface waves' by S. Beji. *Coastal Engineering*, *34*, 163–168.

Kirby, J. T. (2020). Low-order Boussinesq models based on σ coordinate series expansions. *Journal of Fluid Mechanics*, *893*, R3. https://doi.org/10.1017/jfm.2020.376

Lakehal, D., & Liovic, P. (2011). Turbulence structure and interaction with steep breaking waves. *Journal of Fluid Mechanics*, *674*, 522–577.

Lin, P., & Liu, P. L. F. (1999). Internal wavemaker for Navier-Stokes equations models. *Journal of Waterway, Port, Coastal and Ocean Engineering*, *125*(4), 207–215.

Luth, H., Klopman, G., & Kitou, N. (1994). Kinematics of waves breaking partially on an offshore bar; LDV measurements of waves with and without a net onshore current (*Report H-1573*, 40 pp.). Delft: Delft Hydraulics.

Ma, G., Shi, F., & Kirby, J. T. (2011). A polydisperse two-fluid model for surf zone bubble simulation. *Journal of Geophysical Research*, *116*, C05010. https://doi.org/10.1029/2010JC006667

Mase, H., & Kirby, J. T. (1992). Hybrid frequency-domain KdV equation for random wave transformation. In *Coastal Engineering 1992. Proceedings of the International Conference on Coastal Engineering*, (pp. 474–487). Venice: ASCE. https://doi.org/10.1061/9780872629332.035

McCowan, J. (1894). XXXIX. On the highest wave of permanent type. *The London, Edinburgh, and Dublin Philosophical Magazine and Journal of Science*, *38*(233), 351–358. https://doi.org/10.1080/14786449408620643

Melville, W. K. (1996). The role of surface-wave breaking in air-sea interaction. *Annual Review Fluid Mechanics*, *28*, 279–321.

Miche, R. (1944). Breaking wave motion in water of constant depth. *Annales des Ponts et Chaussées*, *121*, 285–319. (in French).

Mivehchi, A. (2018). Experimental and numerical simulations for fluid body interaction problems (Ph.D. Thesis), University of Rhode Island, Narragansett, RI.

Papoutsellis, C. E., Yates, M. L., Simon, B., & Benoit, M. (2019). Modelling of depth-induced wave breaking in a fully nonlinear free-surface potential flow model. *Coastal Engineering*, *154*, 103,579.

Perlin, M, Choi, W, & Tian, Z (2013). Breaking waves in deep and intermediate waters. *Annual Review Fluid Mechanics*, *45*, 115–145.

Pizzo, N., & Melville, W. K. (2019). Focusing deep-water surface gravity wave packets: Wave breaking criteria in a simplified model. *Journal of Fluid Mechanics*, *873*, 238–259.

Rapp, R. J., & Melville, W. K. (1990). Laboratory measurements of deep-water breaking waves. *Philosophical Transactions of the Royal Society A*, *331*, 735–800.

Raubenheimer, B, Guza, R., & Elgar, S. (1996). Wave transformation across the inner surf zone. *Journal of Geophysical Research*, *101*, 25,589–25,597.

Robertson, B., Hall, K., Zytner, R., & Nistor, I. (2013). Breaking waves: Review of characteristic relationships. *Coastal Engineering Journal*, *55*(1), 1,350,002.

Saket, A., Peirson, W. L., Banner, M. L., & Allis, M. J. (2018). On the influence of wave breaking on the height limits of two-dimensional wave groups propagating in uniform intermediate depth water. *Coastal Engineering*, *133*, 159–165.

Saket, A., Peirson, W. L., Banner, M. L., Barthelemy, X., & Allis, M. J. (2017). On the threshold for wave breaking of two-dimensional deep water wave groups in the absence and presence of wind. *Journal of Fluid Mechanics*, *811*, 642–658.

Schäffer, H. A., Madsen, P. A., & Deigaard, R. (1993). A boussinesq model for waves breaking in shallow water. *Coastal Engineering*, *20*, 185–202.

Schwendeman, M., & Thomson, J. (2017). Sharp-crested breaking surface waves observed from a ship-based stereo video system. *Journal of Physical Oceanography*, *47*, 775–792.

Seiffert, B. R., & Ducrozet, G. (2018). Simulation of breaking waves using the high-order spectral method with laboratory experiments: Wave-breaking energy dissipation. *Ocean Dynamics*, *68*, 65–89.

Shemer, L., & Liberzon, D. (2014). Lagrangian kinematics of steep waves up to the inception of a spilling breaker. *Physics of Fluids*, *26*(1), 16,601.

Song, J.-B., & Banner, M. L. (2002). On determining the onset of and strength of breaking for deep water waves. Part I: Unforced irrotational wave groups. *Journal of Physical Oceanography*, *32*, 2541–2558.

Stansell, P., & MacFarlane, C. (2002). Experimental investigation of wave breaking criteria based on wave phase speeds. *Journal of Physical Oceanography*, *32*(5), 1269–1283.

Tanaka, M. (1986). The stability of solitary waves. *The Physics of Fluids*, *29*(3), 650–655.

Tang, S., Yang, Z., Liu, C., Dong, Y.-H., & Shen, L. (2017). Numerical study on the generation and transport of spume droplets in wind over breaking waves. *Atmosphere*, *8*, 248.

Tian, Z., Perlin, M., & Choi, W. (2008). Evaluation of a deep-water wave breaking criterion. *Physics of Fluids*, *20*, 66,604.

Ting, F. C. K., & Kirby, J. T. (1994). Observations of undertow and turbulence in a laboratory surf zone. *Coastal Engineering*, *24*, 51–80.

Ting, F. C. K., & Nelson, J. R. (2011). Laboratory measurements of large-scale near-bed turbulent flow structures under spilling regular waves. *Coastal Engineering*, *58*, 151–172.

Toffoli, A, Babanin, A, Onorato, M., & Waseda, T (2010). Maximum steepness of oceanic waves: Field and laboratory experiments. *Geophysical Research Letter*, *37*, L05603. https://doi.org/10.1029/2009GL041771

Wei, G., Kirby, J. T., Grilli, S. T., & Subramanya, R. (1995). A fully nonlinear Boussinesq model for surface waves. Part 1. Highly nonlinear unsteady waves. *Journal of Fluid Mechanics*, *294*, 71–92.

West, B. J., Brueckner, K. A., Janda, R. S., Milder, D. M., & Milton, R. L. (1987). A new numerical method for surface hydrodynamics. *Journal of Geophysical Research*, *92*, 11,803–11,824.

Wiegel, R. L. (1960). A presentation of cnoidal wave theory for practical application. *Journal of Fluid Mechanics*, *7*, 273–286.

Wu, C. H., & Nepf, H. M. (2002). Breaking criteria and energy losses for three-dimensional wave breaking. *Journal of Geophysical Research*, *107*(C10), 3177.

Yang, Z., Deng, B.-Q., & Shen, L. (2018). Direct numerical simulation of wind turbulence over breaking waves. *Journal of Fluid Mechanics*, *850*, 120–155.